Electronic Supplementary Material (ESI) for Journal of Materials Chemistry A.
This journal is © The Royal Society of Chemistry 2020

Supporting Information

Rational Design of Highly Mesoporous Fe–N–C/Fe_3C/C–S–C Nanohybrid with Dense Active Sites for Superb Electrocatalysis of Oxygen Reduction

Ahmed Al-Shahat Eissa,[a,b,c] Nam Hoon Kim[a,*] and Joong Hee Lee[a,d*]

[a] Department of Nano Convergence Engneering, Jeonbuk National University, Jeonju, Jeonbuk 54896, Republic of Korea

[b] Gradaute School of Energy Science and Technology, Chungnam National University, Yuseong-gu, Daejeon 34134, Republic of Korea

[c] Department of Chemistry, School of Science, South Valley University, Qena 83523, Egypt

[d] Carbon Composite Research Centre, Department of Polymer-Nano Science and Technology, Jeonbuk National University, Jeonju, Jeonbuk 54896, Republic of Korea

* Corresponding authors: nhk@jbnu.ac.kr (Prof. N. H. Kim) and jhl@jbnu.ac.kr (Prof. J. H. Lee)

Experimental section

Materials

All materials were used as received without any further purification. Ammonium ferric oxalate trihydrate ($(NH_4)_3[Fe(C_2O_4)_3].3H_2O$, ≥98% purity), sucrose ($C_{12}H_{22}O_{11}$, ≥99.5% purity), 2-cyanoguanidine ($C_2H_4N_4$, 99.0% purity), dibenzyl disulfide ($C_6H_5CH_2SSH_2C_2C_6H_5$, ≥98.0% purity), thiourea (CH_4N_2S, ≥99.0% purity), sodium sulfide nonahydrate ($Na_2S.9H_2O$, ≥98.0% purity), sodium thiosulfate pentahydrate ($Na_2S_2O_3.5H_2O$, ≥99.5% purity), potassium cyanide (KCN, ≥98.0% purity), perchloric acid ($HClO_4$, 70 wt.%), potassium hydroxide (KOH, ≥85% purity), methanol (CH_3OH, ≥99.9% purity), ethanol (C_2H_5OH, ≥99.8% purity), Nafion solution (5 wt.%), and commercial platinum supported-carbon (Pt/C, 20 wt%) were purchased from Sigma–Aldrich corporation company. Argon, nitrogen, and oxygen gases were provided in cylinders by SIAD Macchine Impianti company with 99.99% purity. Ultrapure deionized water (>18 MΩ cm resistivity) obtained from a Milli-pore Milli-Q system was utilized for the preparation of all aqueous solutions.

Fabrication of electrocatalysts

$C_2H_4N_4$, CH_4N_2S, $C_{12}H_{22}O_{11}$, and $(NH_4)_3[Fe(C_2O_4)_3].3H_2O$ were ground together into a fine powder with percentage ratios of 64, 16, 15, and 5 wt%, respectively for 15 min without the addition of any solvent. The mixture was allowed to completely dry at room temperature. The resulting uniform admixture was placed into an alumina combustion boat, then the boat was put at the center of a horizontal quartz tube furnace and subjected to a temperature-programmed reaction. The mixture was firstly annealed under a flowing argon atmosphere at 550 °C for 1 h, at heating rate of 2 °C min^{-1} then pyrolysed at 850 °C for 1 h, at heating rate of 5 °C min^{-1}. The obtained material was then cooled naturally to room temperature under the protection of Ar atmosphere. After completing the pyrolysis reaction and cooling down, the obtained black material was ground into fine powder and utilized directly without any further processes for the physical characterizations and electrochemical measurements. In order to investigate the influence of S-precursor on the physical and electrochemical properties of the as-synthesized nanomaterial, three additional samples were fabricated under the same conditions except the weight proportion of thiourea was substituted with the same proportion of $C_6H_5CH_2SSH_2C_2C_6H_5$, $Na_2S.9H_2O$, or $Na_2S_2O_3.5H_2O$. For comparative studies

and to explore the effect of S-precursor ratio and hence the S-doping level on the physical and electrocatalytic characteristics of the as-prepared electrocatalyst, extra five samples were synthesized under the same conditions except the weight proportion of CH_4N_2S were altered from 0.0 to 80.0 wt% according to Table S1†.

Materials characterization

Raman spectra were measured at room temperature in the spectral range of 500–3500 cm^{-1} utilizing a Raman Imaging Microscope at 532 nm excitation laser (Tokyo Instruments Co., Nanofinder 30, Japan). A X'PERT POWDER PANalytical diffractometer (Rigaku corporation, D/Max 2500V/PC, Tokyo, Japan) was utilized to identify the crystalline properties and nature of phases existed within the as-synthesized materials using Cu (Kα mean) radiation (λ = 1.5419 Å). The 2θ angles were extended from 10° to 80° using a scan step size of 0.033° and scanning rate of 2° min^{-1}. N_2–physisorption isotherms were measured at 77 K on an adsorption volumetric analyzer by Micromeritics ASAP 2020 Accelerated Surface Area & Porosimetry System instrument. All samples were degassed at 180 °C under vacuum for 6 h before the N_2 adsorption–desorption measurements. The specific surface areas (SSAs) were calculated by the Brunauer–Emmett–Teller (BET) method. The micropore volumes were evaluated utilizing the *t*-plot method. The average pore size distribution (PSD) curves were measured with the Barrett–Joyner–Halenda (BJH) method, based on the analysis of the desorption branch of the isotherm. The total pore volume was estimated from the quantity of adsorbed N_2 at a relative pressure of 0.99. Scanning electron microscopy (SEM) images were recorded using a field emission SEM (FE-SEM; SUPRA 40 VP; Carl Zeiss, Germany) located at the Center for University Wide Research Facilities (CURF), Jeonbuk National University, South Korea. The X–ray photoelectron spectroscopy (XPS) patterns were recorded by using Theta Probe AR–XPS System (Thermo Fisher Scientific, UK) with a monochromatic X–ray source (Al $K\alpha^+$) located at the Korea Basic Science Institute (KBSI, Busan), to identify the elemental constituents and their proportions in the surface region of the as-synthesized nanomaterials. Transmission electron microscopy (TEM), high resolution TEM (HRTEM), and high-angle annular dark field scanning TEM (HAADF-STEM) were performed by JEM–2200FS instrument (JEOL Co., USA) operated at working voltage of 200 kV, located at the Korea Basic Science Institute (KBSI, Jeonju). The samples

were prepared for imaging by dispersing the catalyst powder in ultrapure ethanol and making sonication for 1 h, then dropping the diluted ethanolic-suspension solution of the catalyst onto a carbon microgrid corroborative by a 300-mesh copper grid.

Electrochemical measurements

The electrochemical performances of the as-synthesized electrocatalysts were carried out in a conventional three-electrode system using an electrochemical workstation machine (CH660E Instruments, Inc., USA) equipped with a glassy carbon rotating disk electrode (RDE) at room temperature (298 *K*). A platinum foil and a saturated calomel electrode (SCE) were used as counter and reference electrodes, respectively. Rotating disk electrode (RDE, 3.0 mm diameter, 0.0706 cm^2, PINE Instrument Inc.) coated with the electrocatalyst film was utilized as a working electrode. Before dropping the catalyst ink on the electrode surface, the glassy carbon (GC) electrode was successively polished with alumina powders having an average size of 0.5, 0.15, and 0.05 μm (CH Instrument Inc.), to fully clean any impurities on the electrode surface, then rinsed with ultrapure water and ethanol to remove the alumina powder. The electrocatalysts suspensions were prepared by dispersing 5.0 mg of the catalyst in 0.5 mL solution containing 145 μL of ethanol, 345 μL of deionized water followed by ultrasonication for 40 min. Thereafter, 10 μL of Nafion (0.5 wt%) were added to the previous mixture to enhance the dispersion of the catalyst suspension and improve the binding with the GC electrode surface, then the mixture was ultrasonicated again for a certain time until getting a homogeneous suspension. A commercial carbon-supported platinum (Pt/C, 20 wt%) electrode was prepared following the same procedure, as a reference catalyst. Subsequently, a certain amount of the as-prepared ink was dropped onto the GC electrode surface, then dried in air at room temperature resulting in a loading of 300 μg cm^{-2} for Fe–N–C/Fe_3C/C–S–C electrocatalysts and Pt/C (60 μg_{Pt} cm^{-2}).

The CV measurements were performed either in 0.10 M KOH electrolyte in the potential window from –0.80 to 0.20 V or in 0.10 M $HClO_4$ electrolyte in the potential window from –0.20 to +0.80 V vs SCE electrode at a scanning rate of 50 mV s^{-1} using the CH660E machine. Before examining the electrocatalysts, the electrolyte solution was bubbled with the highly pure nitrogen or oxygen for 30 min with a flowing rate of 100 mL/min to ensure a full saturation with gases. The working electrode was cycled and activated for at least 100 cycles at scan rate of 50 mV s^{-1} in N_2–saturated 0.10 M KOH or 0.10 M $HClO_4$ solutions before collecting the data in N_2–saturated

electrolytes, then cycled again for another 100 cycles at the same scan rate in O_2–saturated electrolytes before collecting the data in O_2–saturated electrolytes, to obtain stable and reproducible signals. All the potentials were measured vs SCE then converted to the reversible hydrogen electrode (RHE) scale according to Nernst equation:

$$E_{RHE} = E_{SCE} + 0.059pH + E^{\circ}_{SCE}$$

where E_{RHE} is the converted potential vs RHE, E_{SCE} is the experimentally recorded potential vs SCE, and E°_{SCE} is the standard potential of SCE at 25 °C (0.244 V).

Linear sweep voltammetry (LSV) measurements were implemented in O_2–saturated 0.10 M KOH, or in O_2–saturated 0.10 M $HClO_4$ electrolytes at various rotation rates from 400 to 3200 rpm at scan rate of 5 mV s^{-1}, to study the ORR performance of the prepared materials. All currents were corrected for the background current measured in N_2–saturated electrolyte. The current densities were normalized by the geometric surface area of the glassy carbon electrode. The onset potential (E_0) was defined as the potential at which the current density exceeded a threshold value of 0.10 mA cm^{-2}, meanwhile the half–wave potential ($E_{1/2}$) is the potential which corresponds to 50% of the diffusion–limiting current density (J_L). J_L was calculated at the potential of 0.30 V vs RHE. The number of electrons transferred (n) was calculated from the slopes of the fitted linear curves based on the detailed analysis the Koutecky–Levich (K–L) equation at different electrode potentials, where the relation between J^{-1} and $\omega^{-1/2}$ was plotted:

$$\frac{1}{J} = \frac{1}{J_K} + \frac{1}{J_L} = \frac{1}{J_K} + \frac{1}{B\omega^{1/2}}$$

$$B = 0.62nFC_{O_2}(D_{O_2})^{2/3}\nu^{-1/6}$$

$$J_K = nFkC_{O_2}$$

Where, J is the measured current density at a specific potential, J_K is the kinetic current density, J_L is the diffusion-limiting current density , ω is the electrode angular rotation speed in rad/s ($\omega = 2\pi N$, N is the linear rotation speed), B is related to diffusional current density, and can be calculated from the slopes of the K–L plots based on the K–L equation (B is the reciprocal of slope), n represents the number of electrons transferred per oxygen (O_2) molecule, F is the Faraday constant (F = 96485 C

mol^{-1}), C_{O_2} is the bulk concentration of O_2 (1.20×10^{-3} mol L^{-1} in 0.10 M KOH aqueous solution and 1.26×10^{-3} mol L^{-1} in 0.10 M $HClO_4$ aqueous solution), D_{O_2} is the diffusion coefficient of O_2 (1.90×10^{-5} cm^2 s^{-1} in 0.10 M KOH solution and 1.93×10^{-5} cm^2 s^{-1} in 0.10 M $HClO_4$ solution), and v is the kinematic viscosity of the electrolyte (0.01 cm^2 s^{-1} for both 0.10 M KOH and 0.10 M $HClO_4$ aqueous solutions). The coefficient 0.62 is indicated as the conversion factor for the rotation velocity expressed in revolutions per minute (rpm). In Tafel plots (E vs log J_k), the kinetic current density was determined from the mass-transport correction of the RDE based on the K–L equation:

$$J_K = \frac{J \times J_L}{J_L - J}$$

The accelerated durability test (ADT) for Fe–N–C/Fe_3C/C–S–C and the state-of-the-art Pt/C (20 wt%) electrocatalysts were carried out by the potential cycling of the working electrode from 0.40 to 1.1 V vs RHE, in O_2–saturated 0.10 M KOH or 0.10 M $HClO_4$ electrolytes for a continuous 15,000 potential cycles at a scan rate of 100 mV s^{-1} that can provide harsh degradation conditions. After finishing the cyclic stability test, the active material loaded on the working electrode was undergone to the polarization tests, and the variations in the E_0, $E_{1/2}$, and J_L before and after 15,000 cycles were calculated. In addition, the long-term durability test was evaluated by the chronoamperometric test for 50 h, at 0.70 V vs RHE at a rotation rate of 1600 rpm. The methanol tolerance experiments were conducted by chronoamperometric measurements. The chronoamperometric responses were carried out for 10,000 s at 0.70 V vs RHE and rotation speed of 1600 rpm, in O_2–saturated 0.10 M KOH or 0.10 M $HClO_4$ electrolytes.

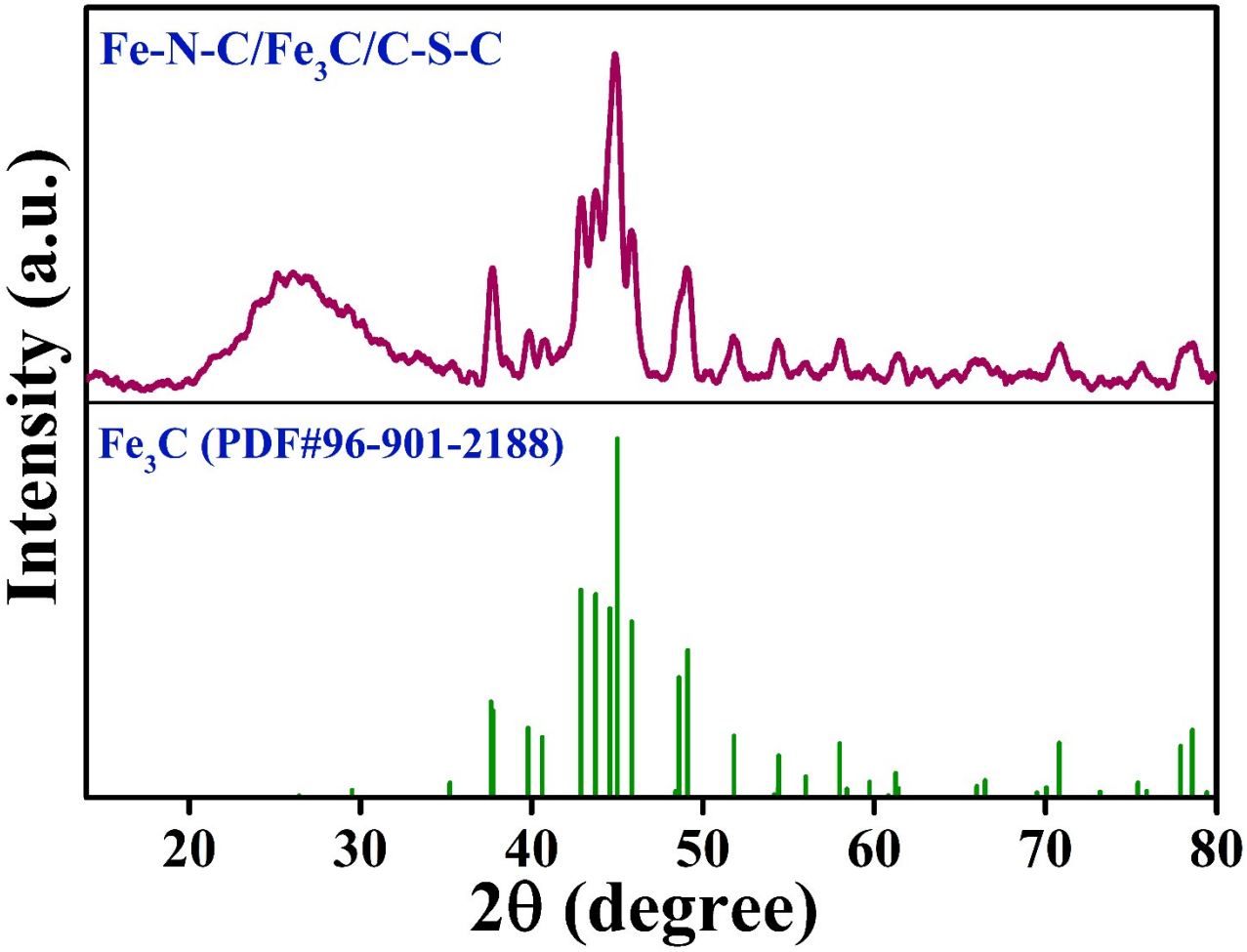

Fig. S1 Powder XRD profile of Fe–N–C/Fe_3C/C–S–C nanohybrid with respect to the reference phase.

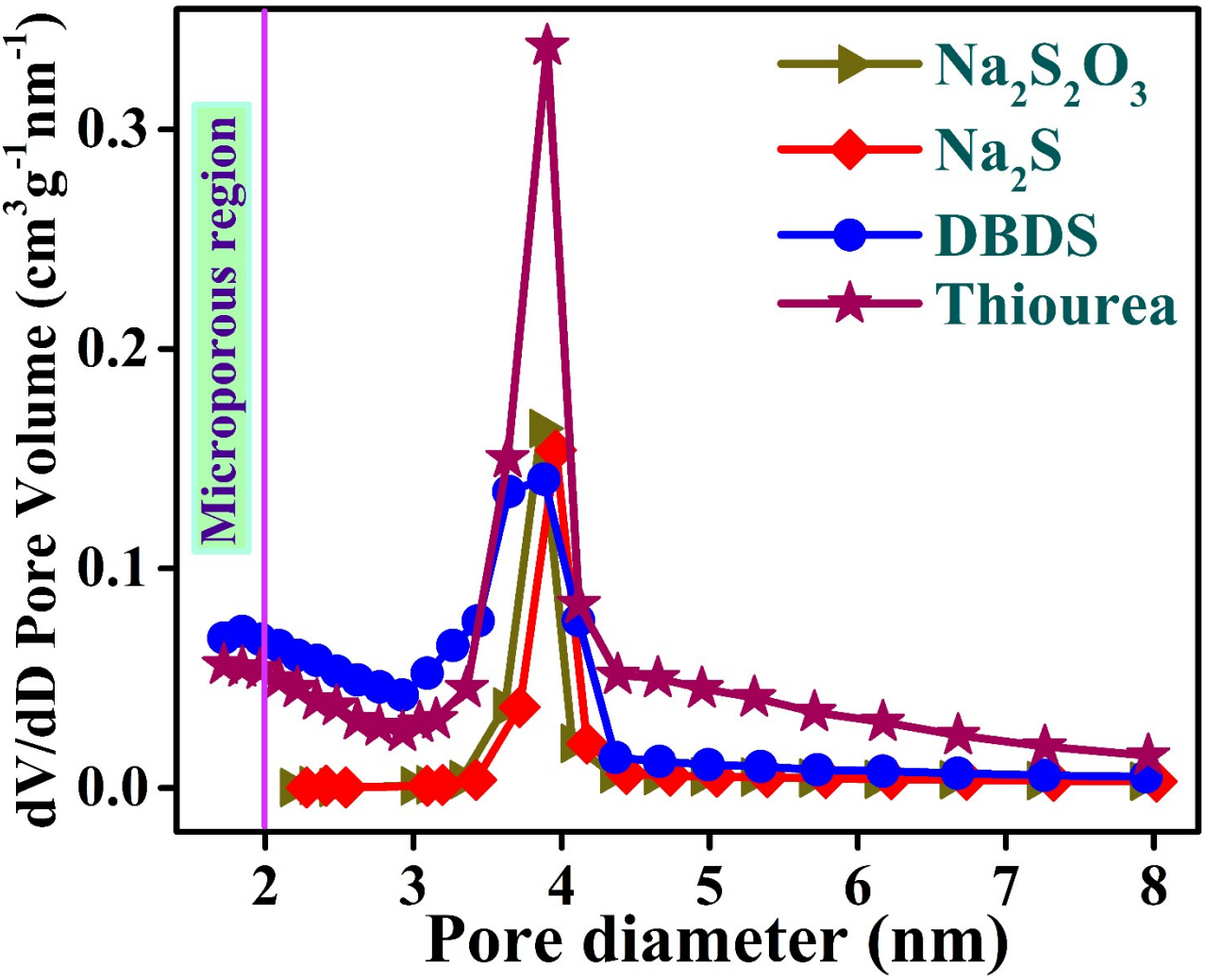

Fig. S2 Pore size distribution plots of Fe–N–C/Fe_3C/C–S–C nanohybrids synthesized using various S precursors.

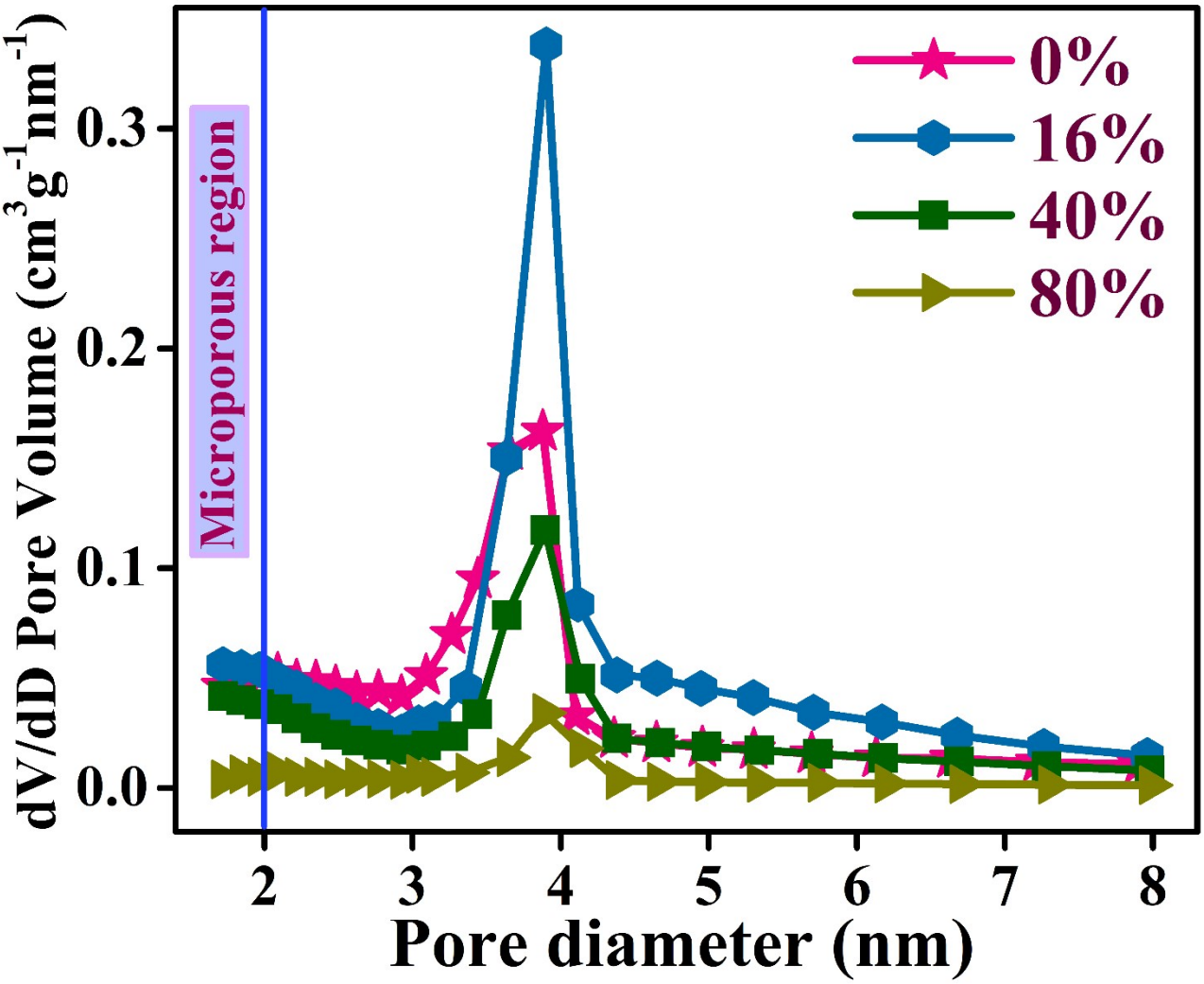

Fig. S3 Pore size distribution plots of Fe–N–C/Fe_3C/C–S–C nanohybrids fabricated utilizing different proportions of thiourea precursor.

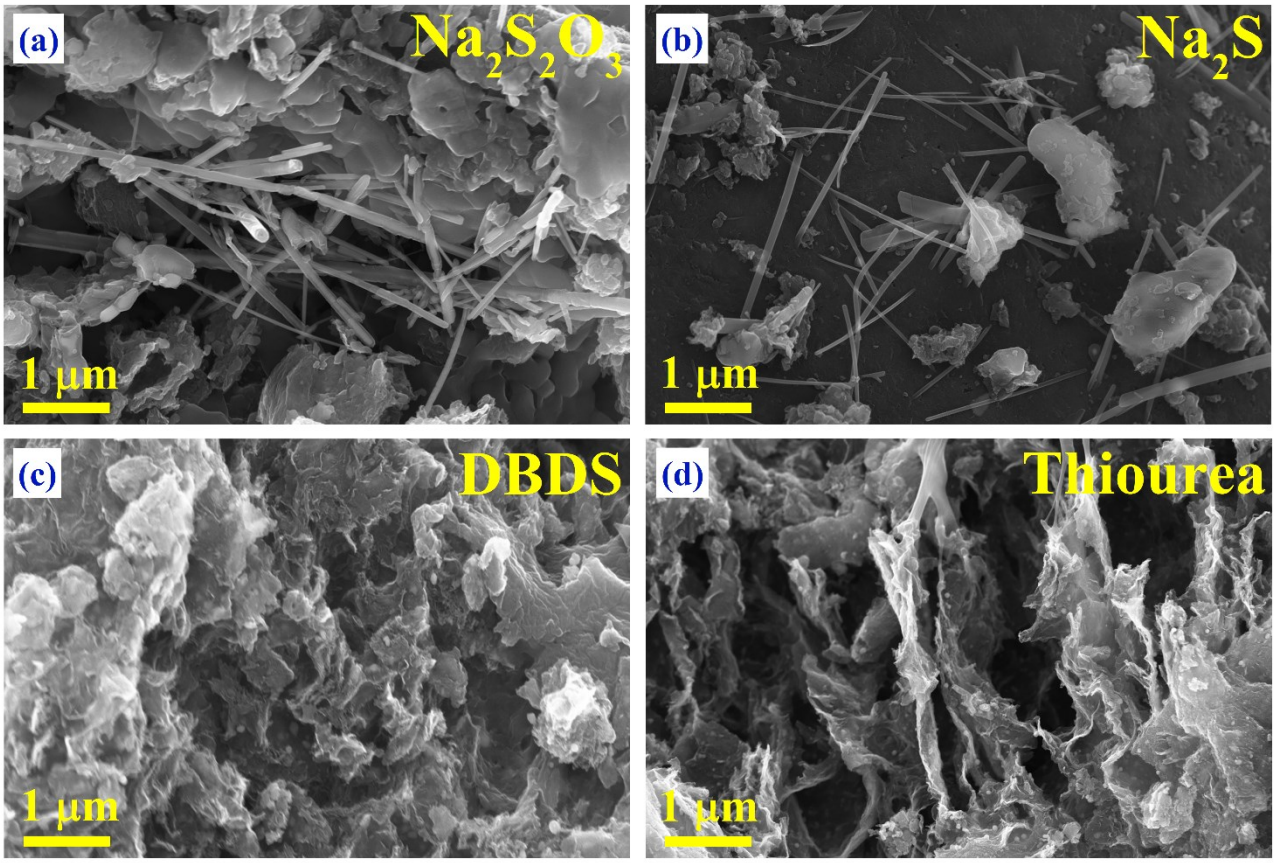

Fig. S4 FESEM images at low magnifications of Fe–N–C/Fe_3C/C–S–C nanohybrids fabricated using various S precursors.

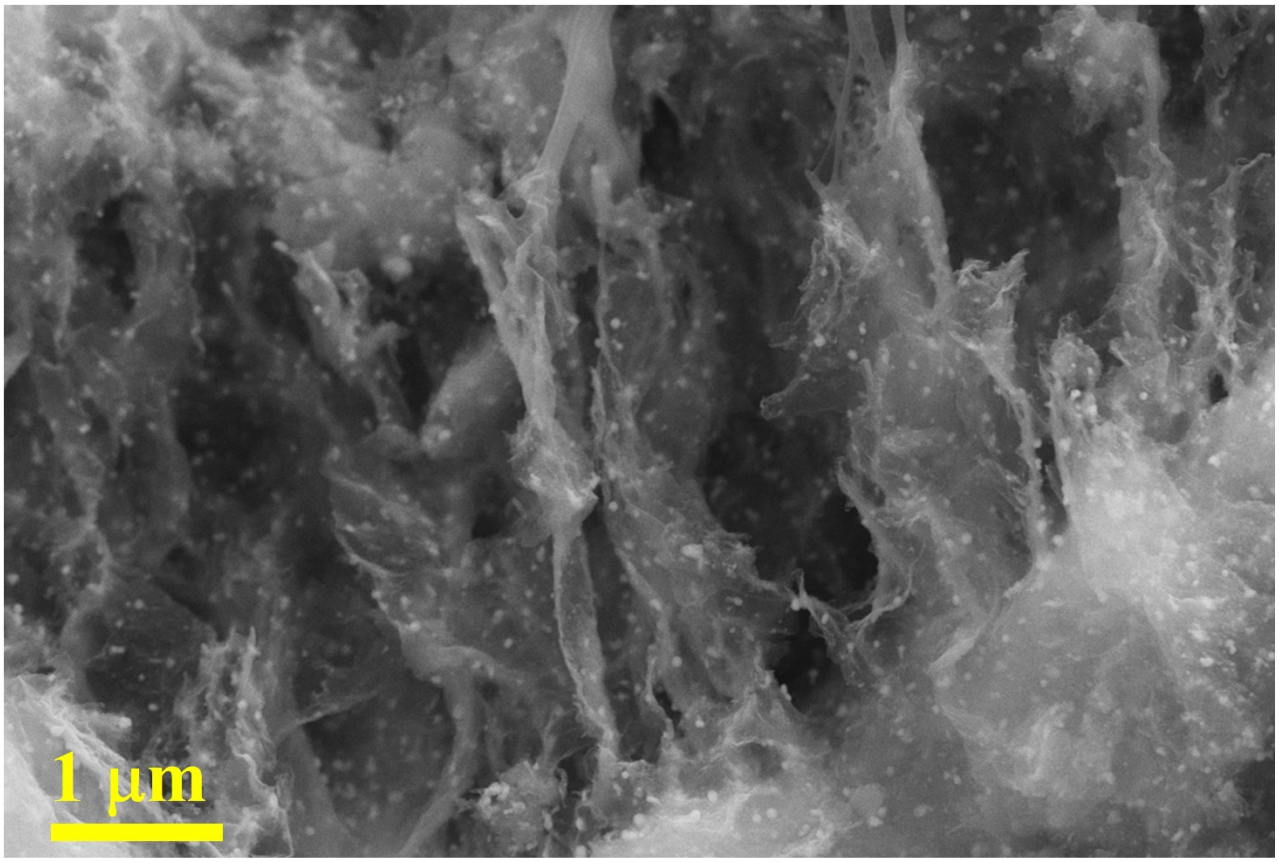

Fig. S5 FESEM image at low magnification of Fe–N–C/Fe_3C/C–S–C nanohybrid fabricated utilizing thiourea, showing the homogenous dispersion of the NPs.

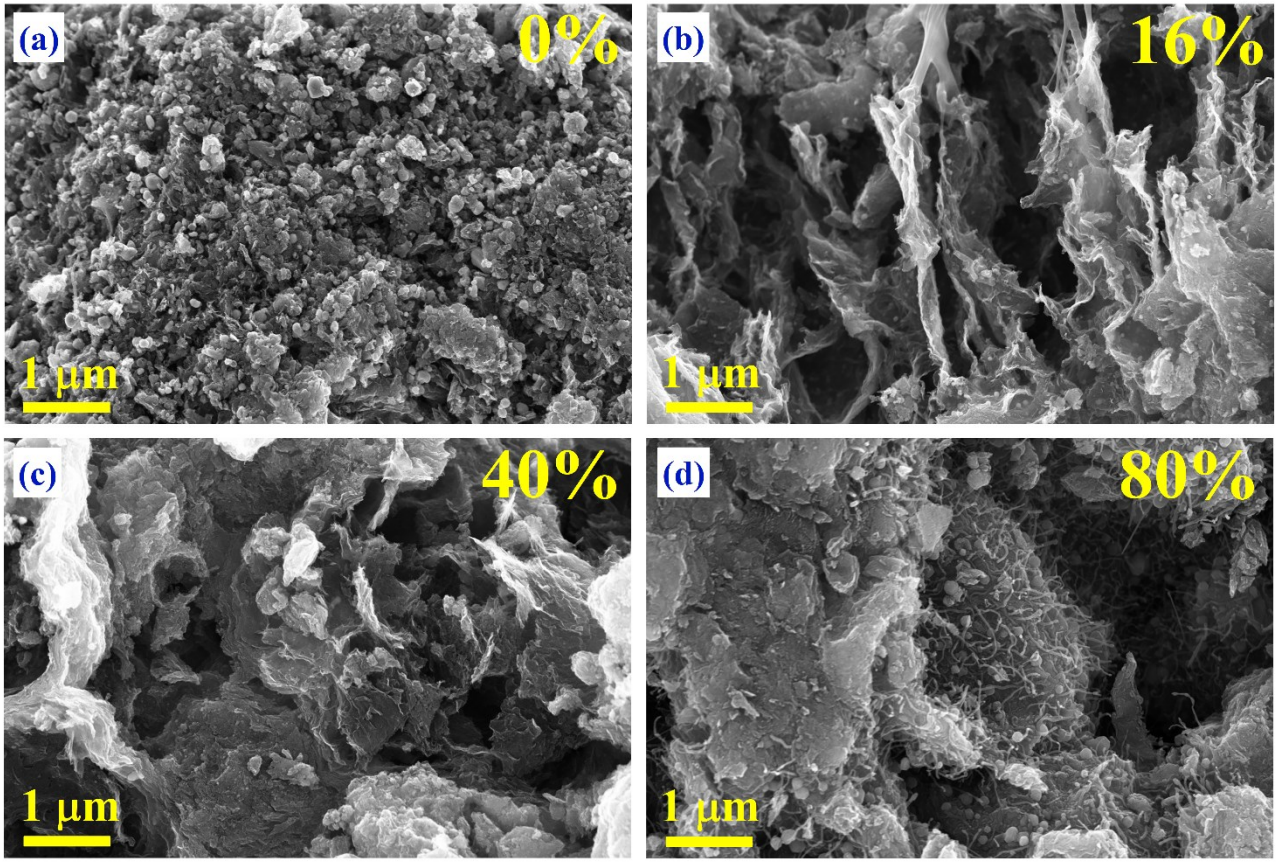

Fig. S6 FESEM images at low magnifications of Fe–N–C/Fe_3C/C–S–C nanohybrids prepared using different proportions of thiourea precursor.

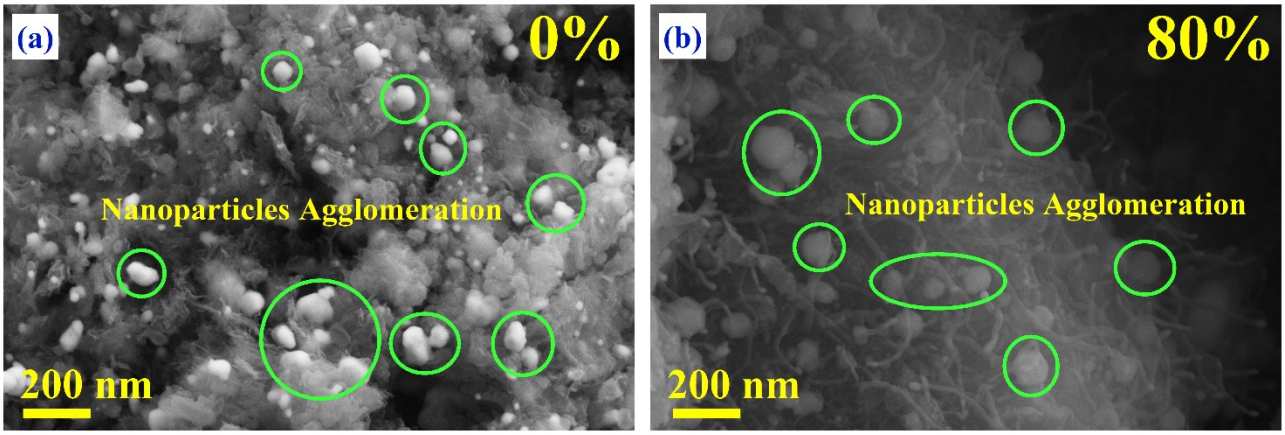

Fig. S7 FESEM images of the electrocatalysts synthesized without S-doping (a), and in the presence of high ratio of thiourea (80 wt%) (b). The green circles show the agglomerated NPs.

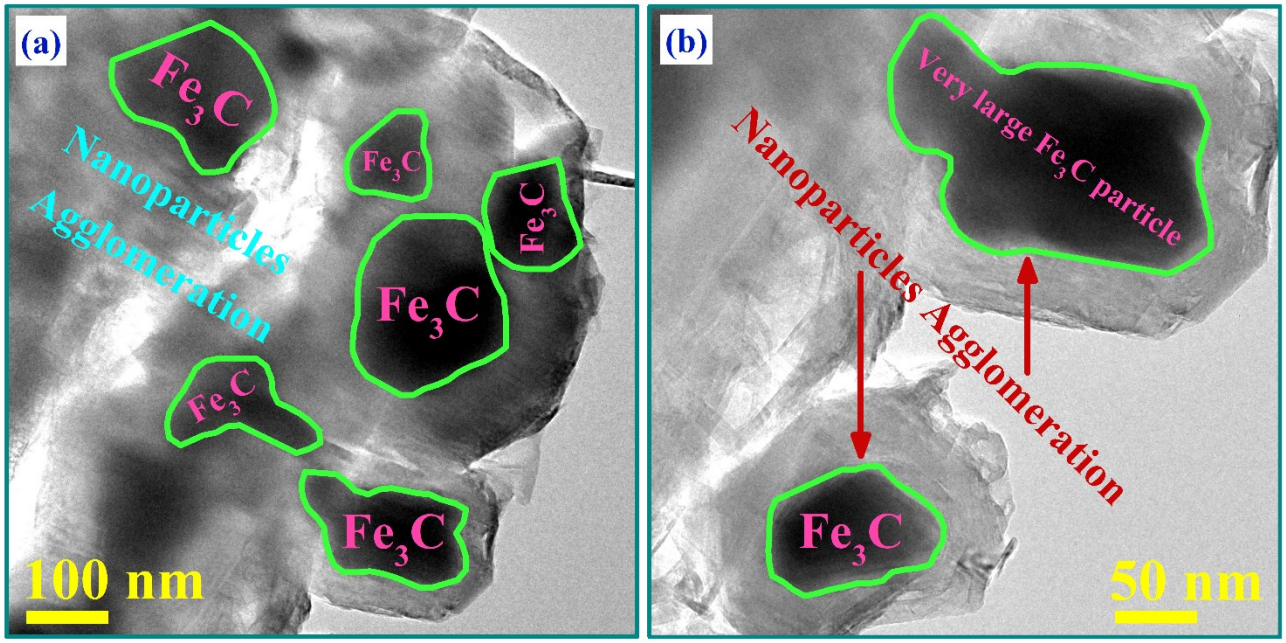

Fig. S8 TEM images at different magnifications of the electrocatalyst fabricated using $Na_2S_2O_3$ precursor.

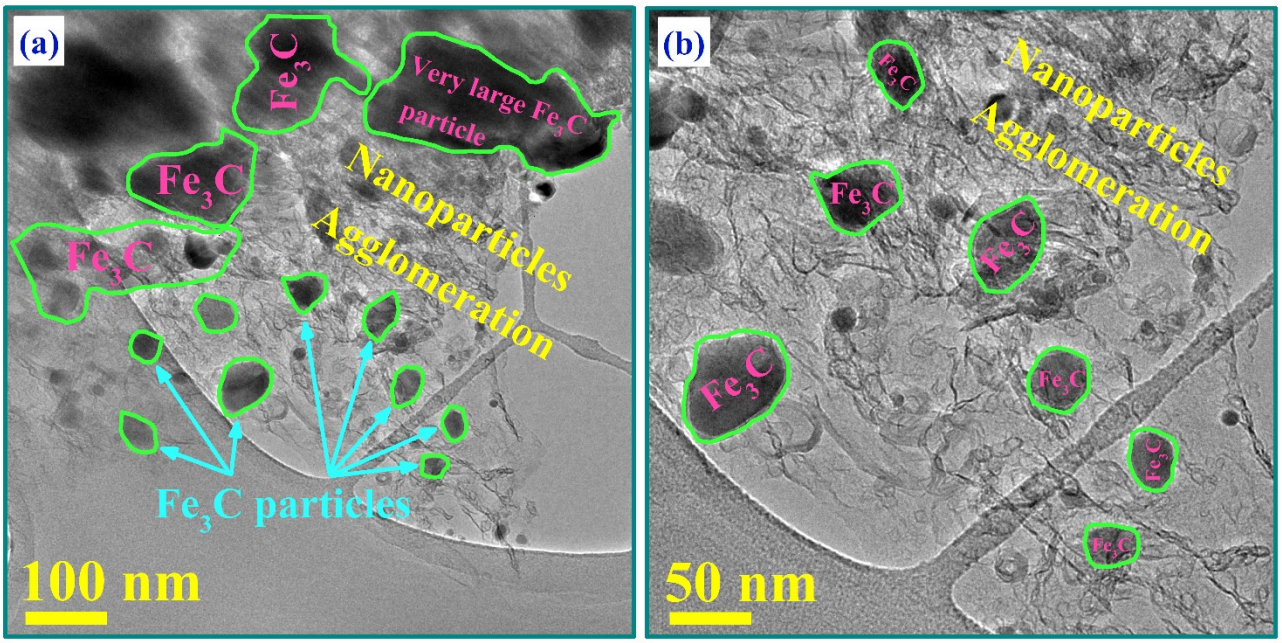

Fig. S9 TEM images at different magnifications of the electrocatalyst fabricated without S-doping.

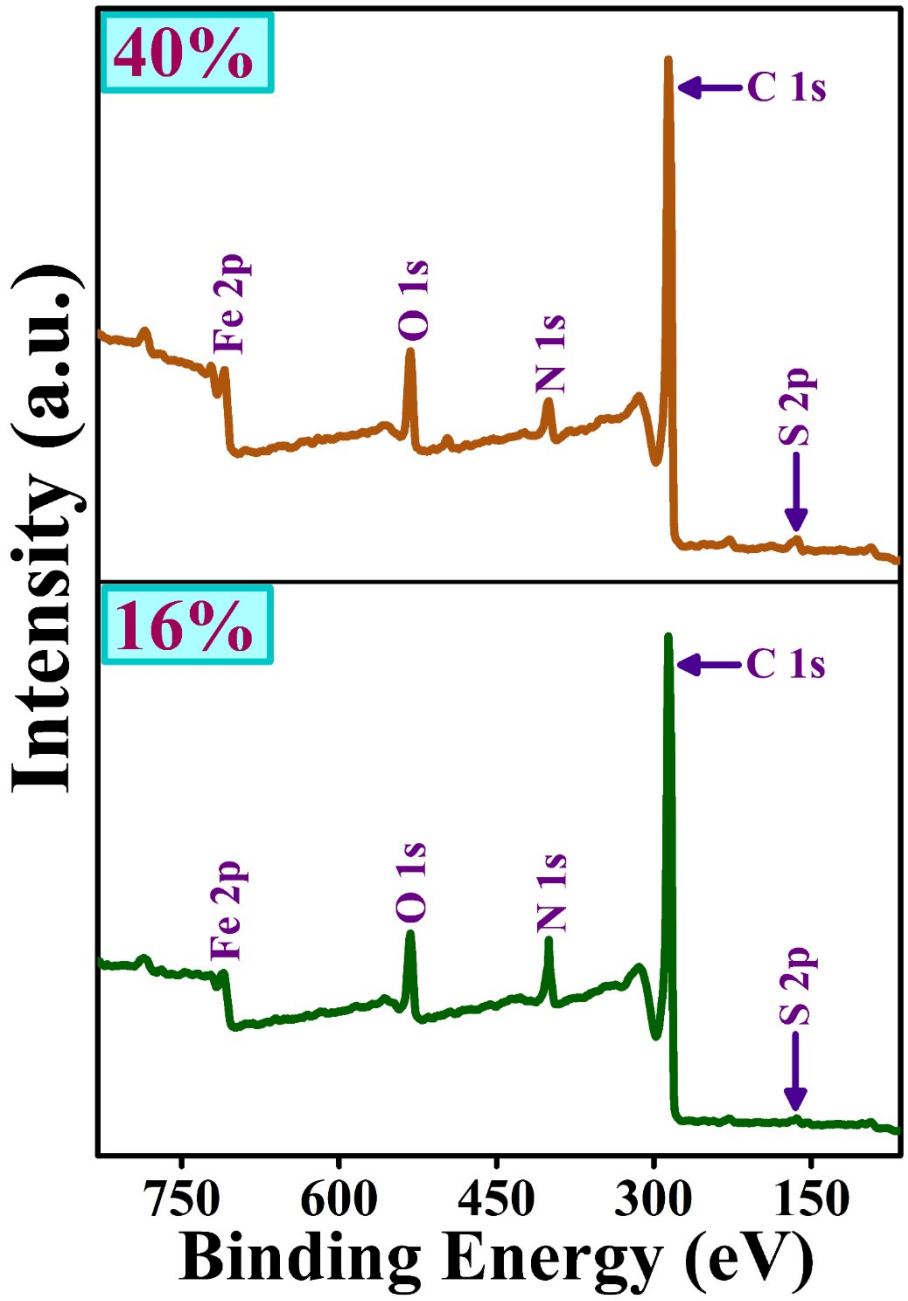

Fig. S10 XPS survey spectrum of Fe–N–C/Fe_3C/C–S–C nanohybrids synthesized using 16 and 40 wt% of thiourea.

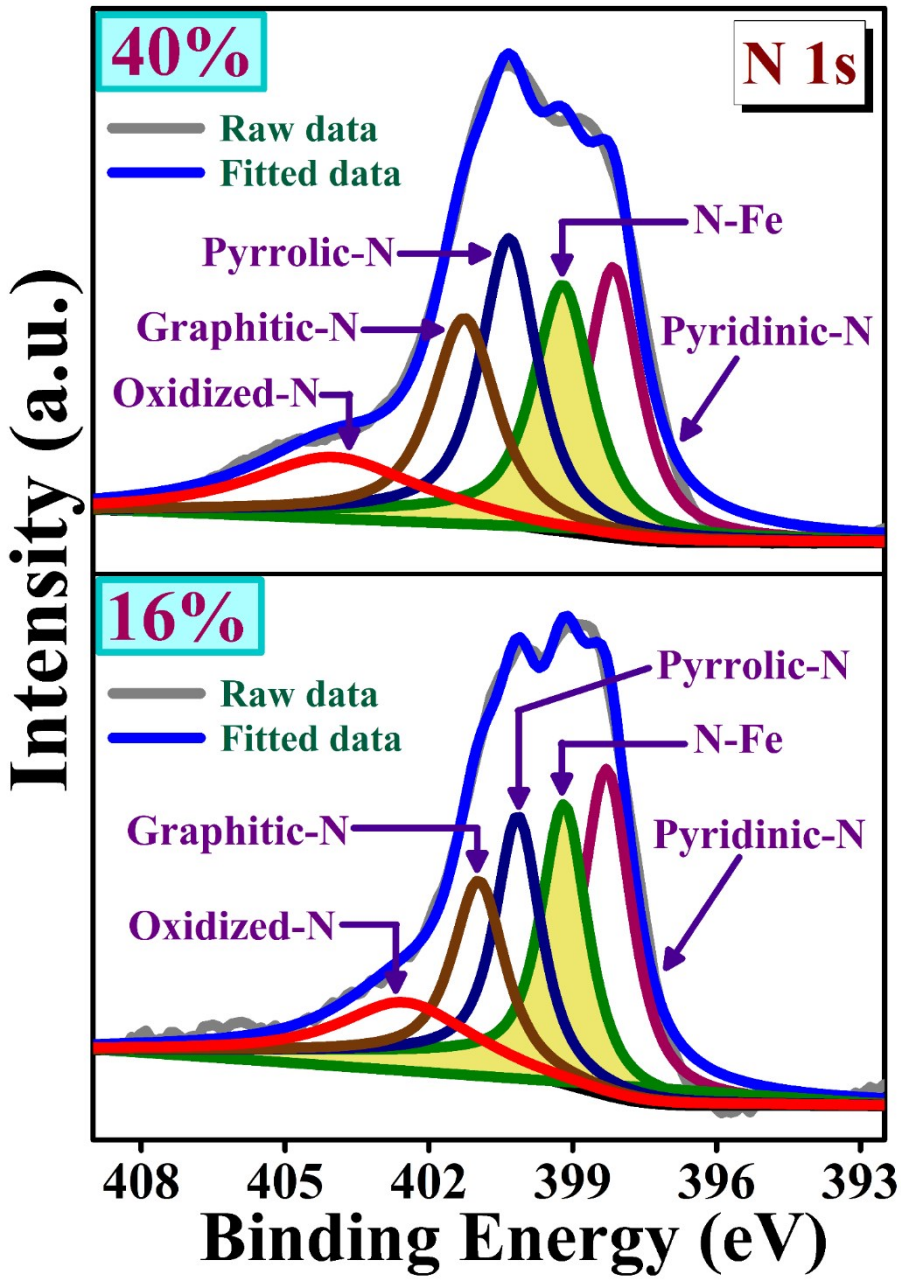

Fig. S11 Fitted high-resolution XPS spectra of the N 1s in Fe–N–C/Fe_3C/C–S–C nanohybrids synthesized using 16 and 40 wt% of thiourea.

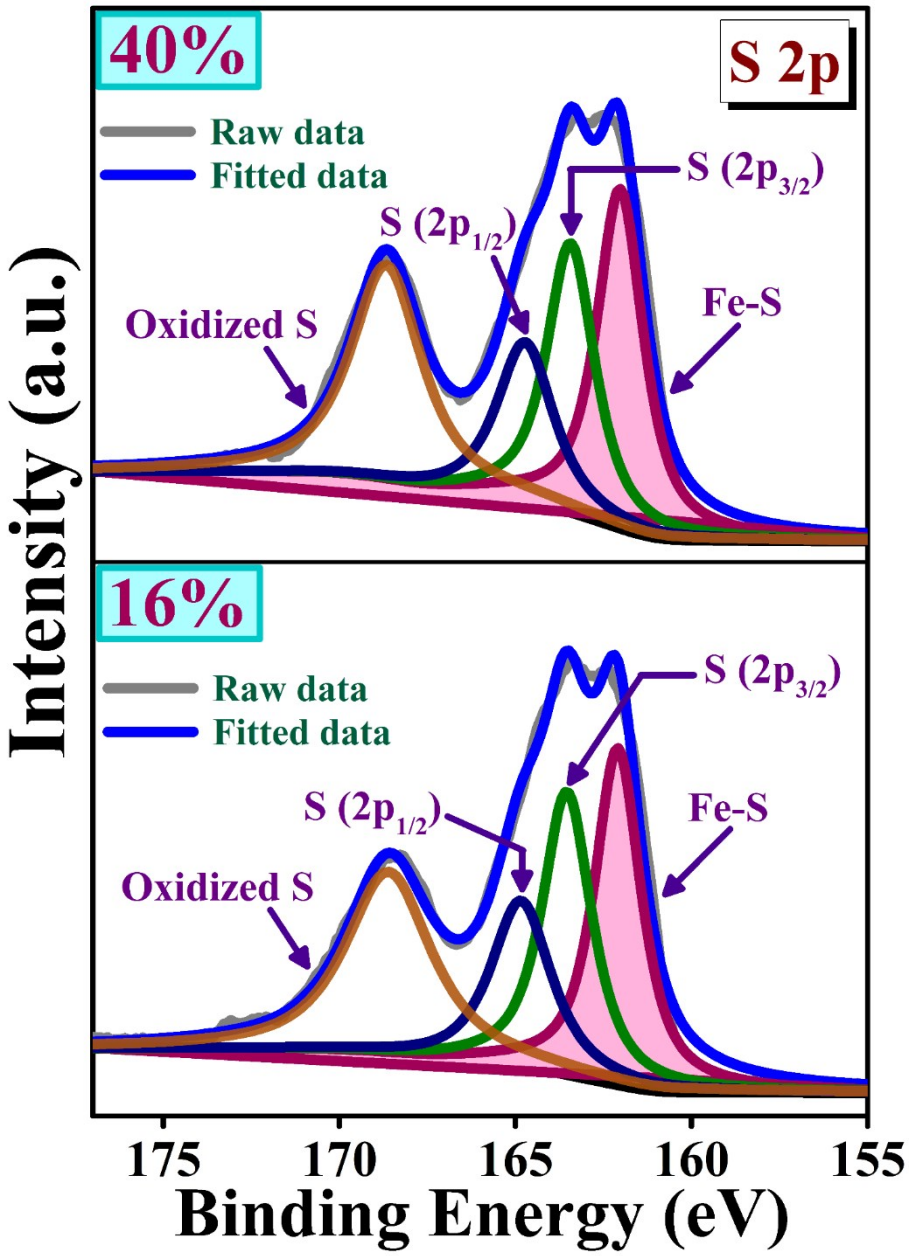

Fig. S12 Fitted high-resolution XPS spectra of the S 2p in Fe–N–C/Fe_3C/C–S–C nanohybrids prepared utilizing 16 and 40 wt% of thiourea.

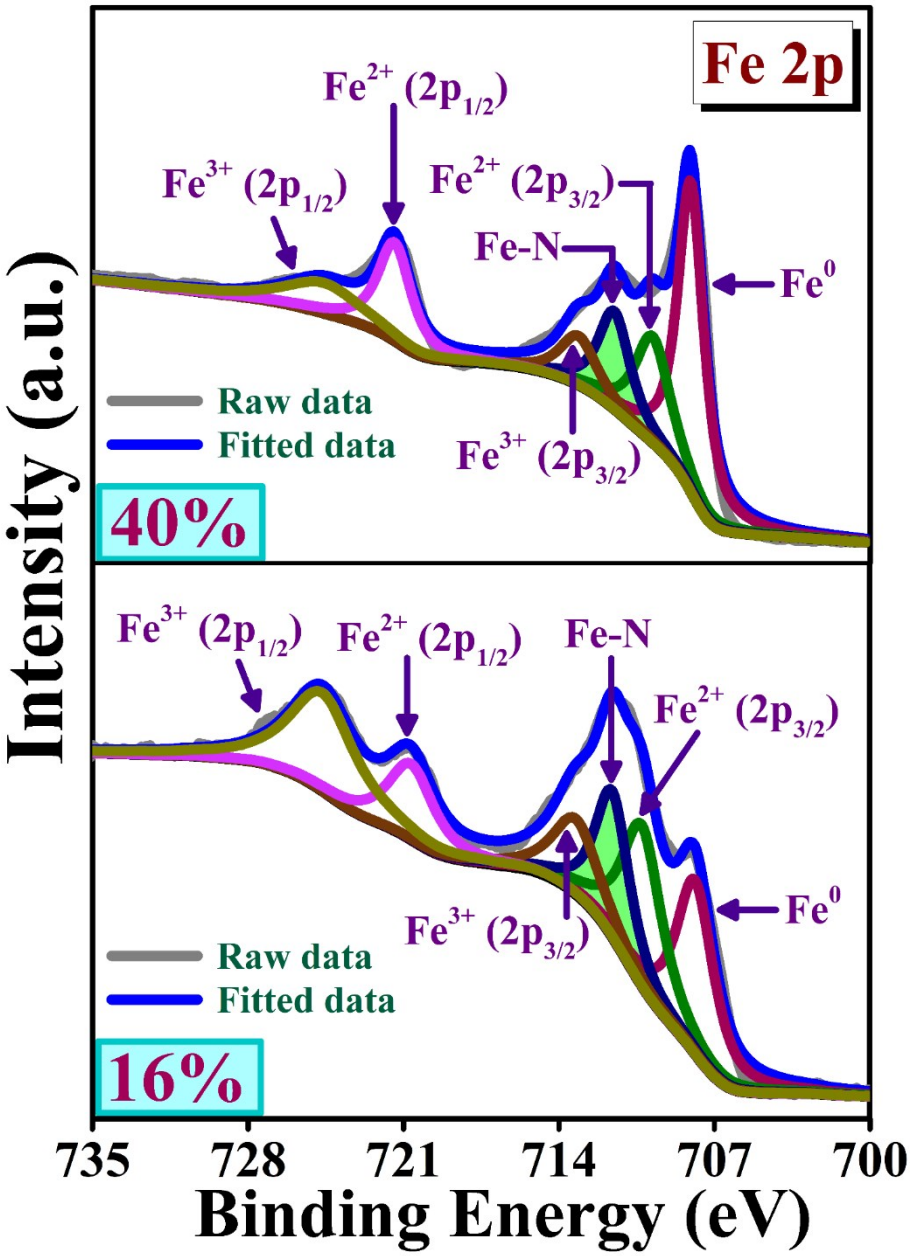

Fig. S13 Fitted high-resolution XPS spectra of the Fe 2p in Fe–N–C/Fe_3C/C–S–C nanohybrids fabricated utilizing 16 and 40 wt% of thiourea.

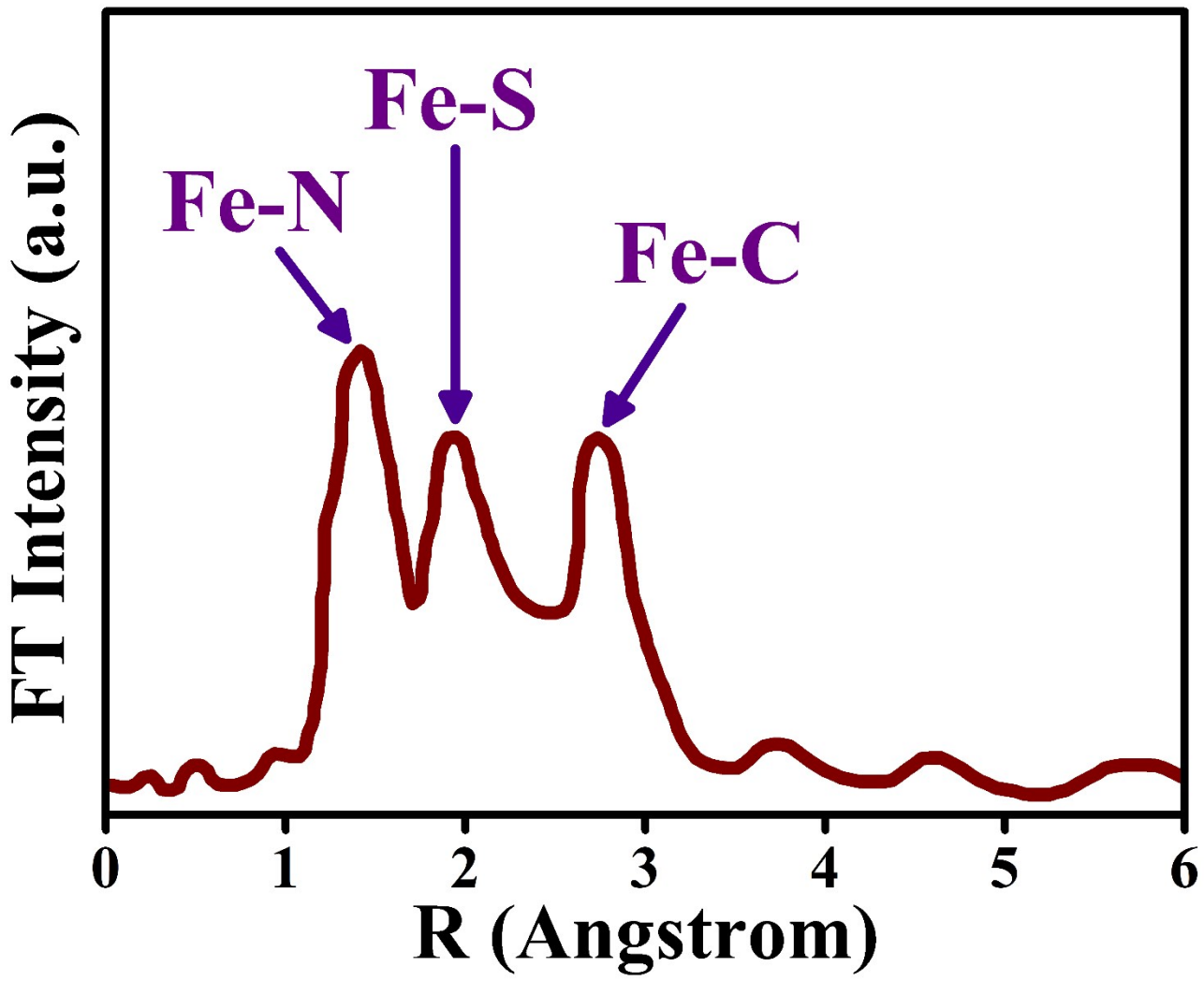

Fig. S14 Fourier transform of the EXAFS spectra in R-space of Fe–N–C/Fe_3C/C–S–C nanohybrid. R is the distance in Angstrom

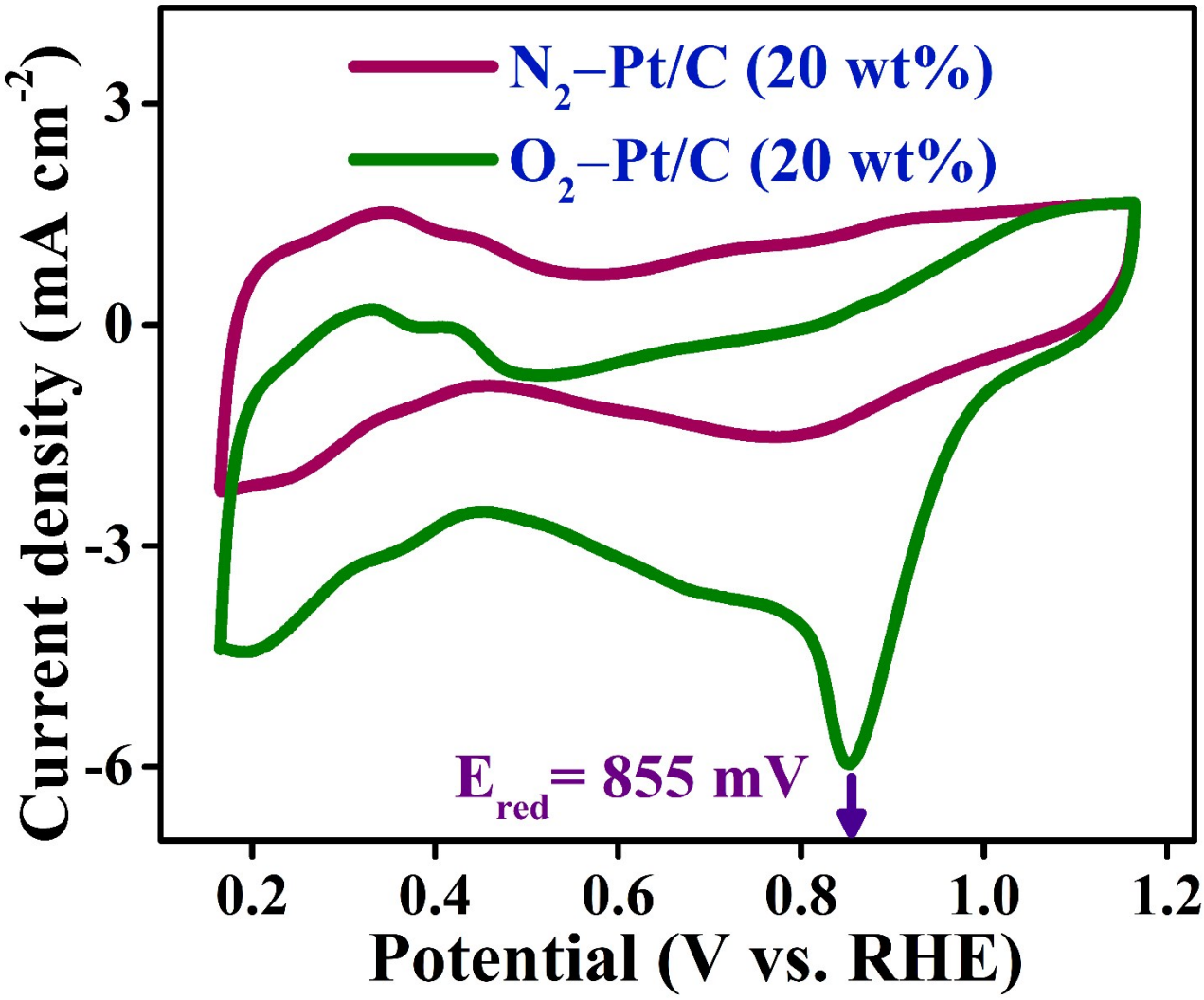

Fig. S15 CV curves of the state-of-the-art Pt/C (20 wt%), in N_2– and O_2–saturated 0.10 M KOH solution at scan rate of 50 mV s^{-1}.

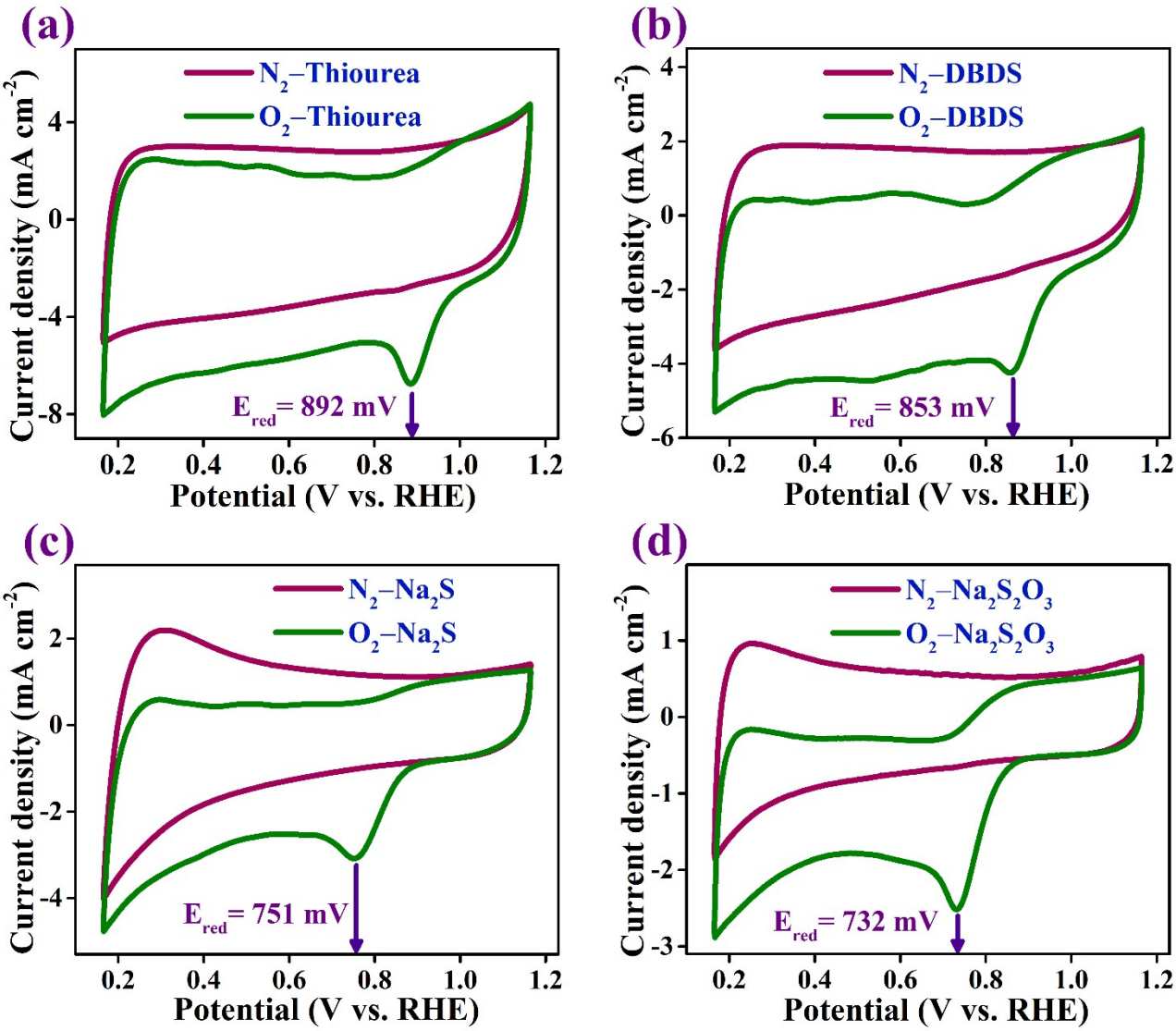

Fig. S16 CV curves of Fe–N–C/Fe_3C/C–S–C nanohybrids fabricated using different S precursors, in N_2– and O_2–saturated 0.10 M KOH solution at scan rate of 50 mV s^{-1}.

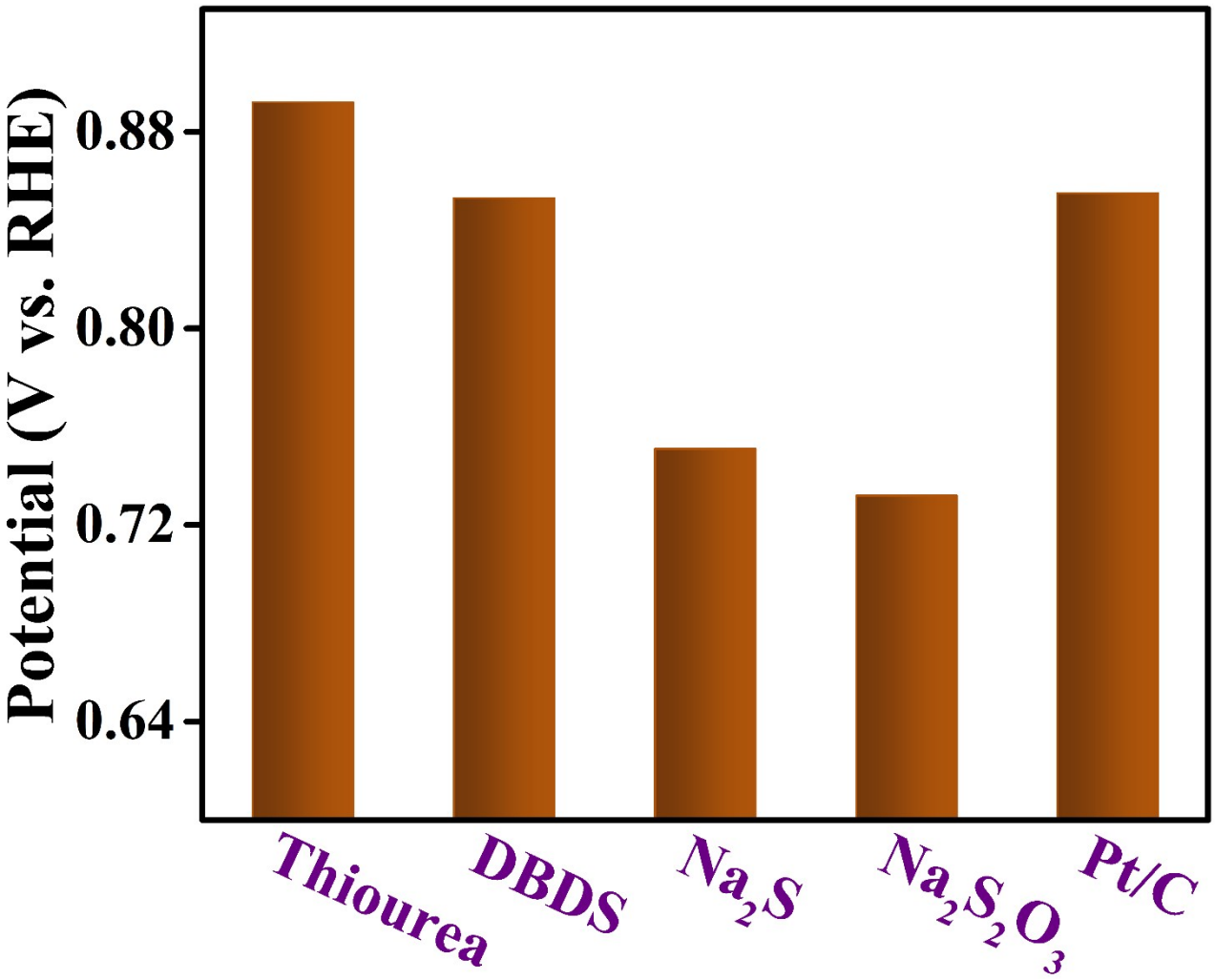

Fig. S17 Relation between the utilized S precursor and the reduction peak potential.

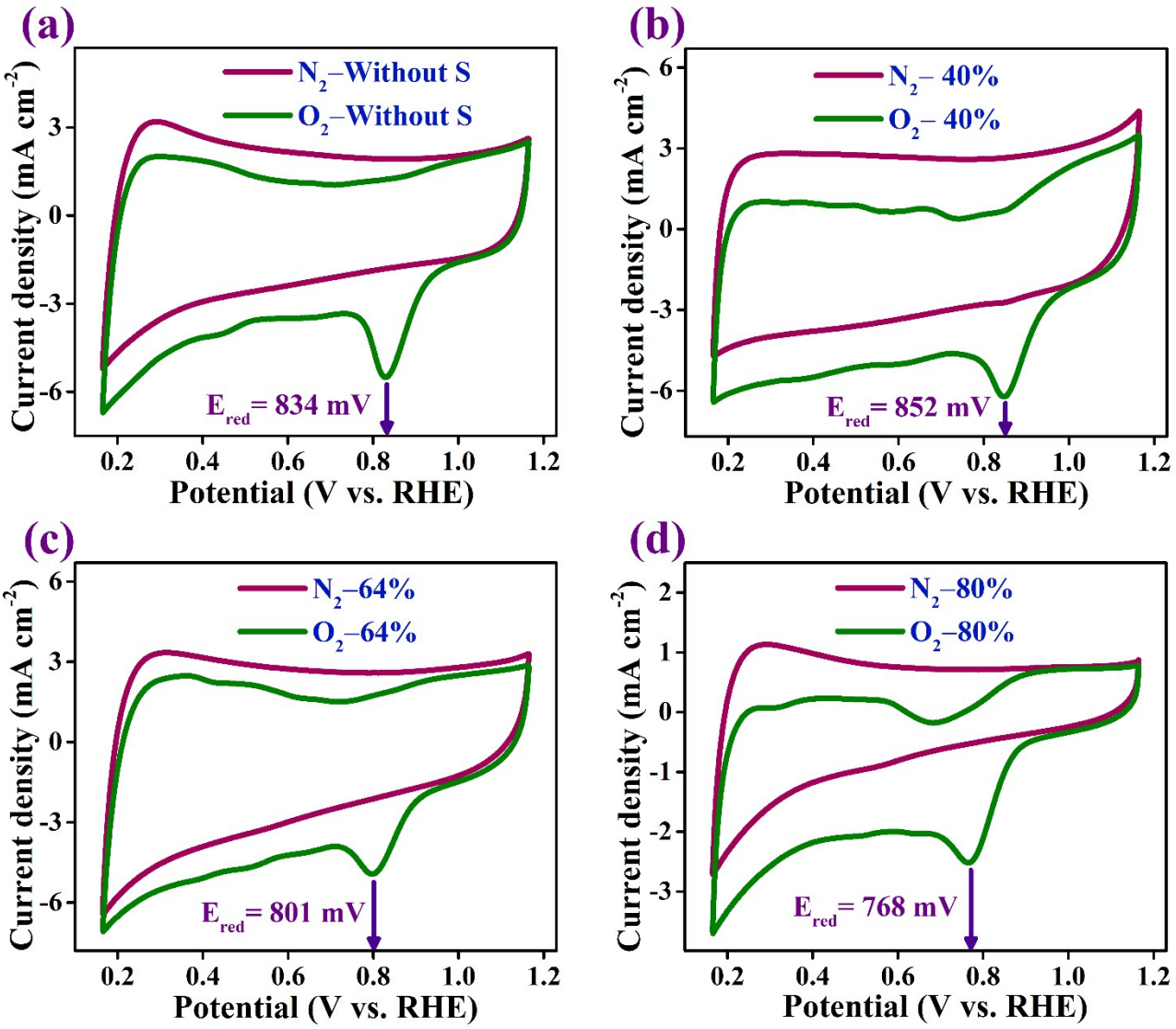

Fig. S18 CV curves of Fe–N–C/Fe_3C/C–S–C nanohybrids synthesized using various proportions of thiourea, in N_2– and O_2–saturated 0.10 M KOH solution at scan rate of 50 mV s^{-1}.

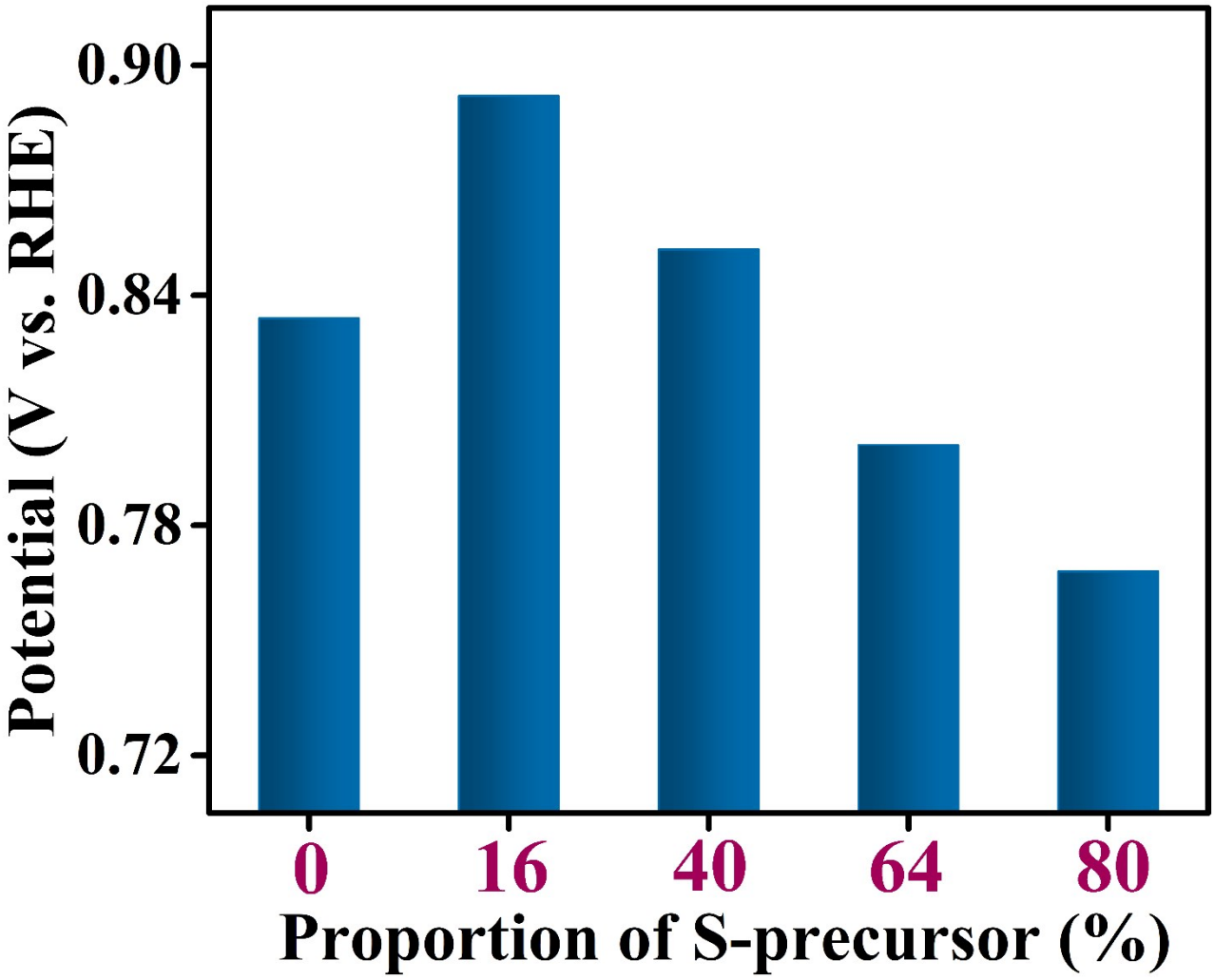

Fig. S19 Relation between the weight proportion of thiourea and the reduction peak potential.

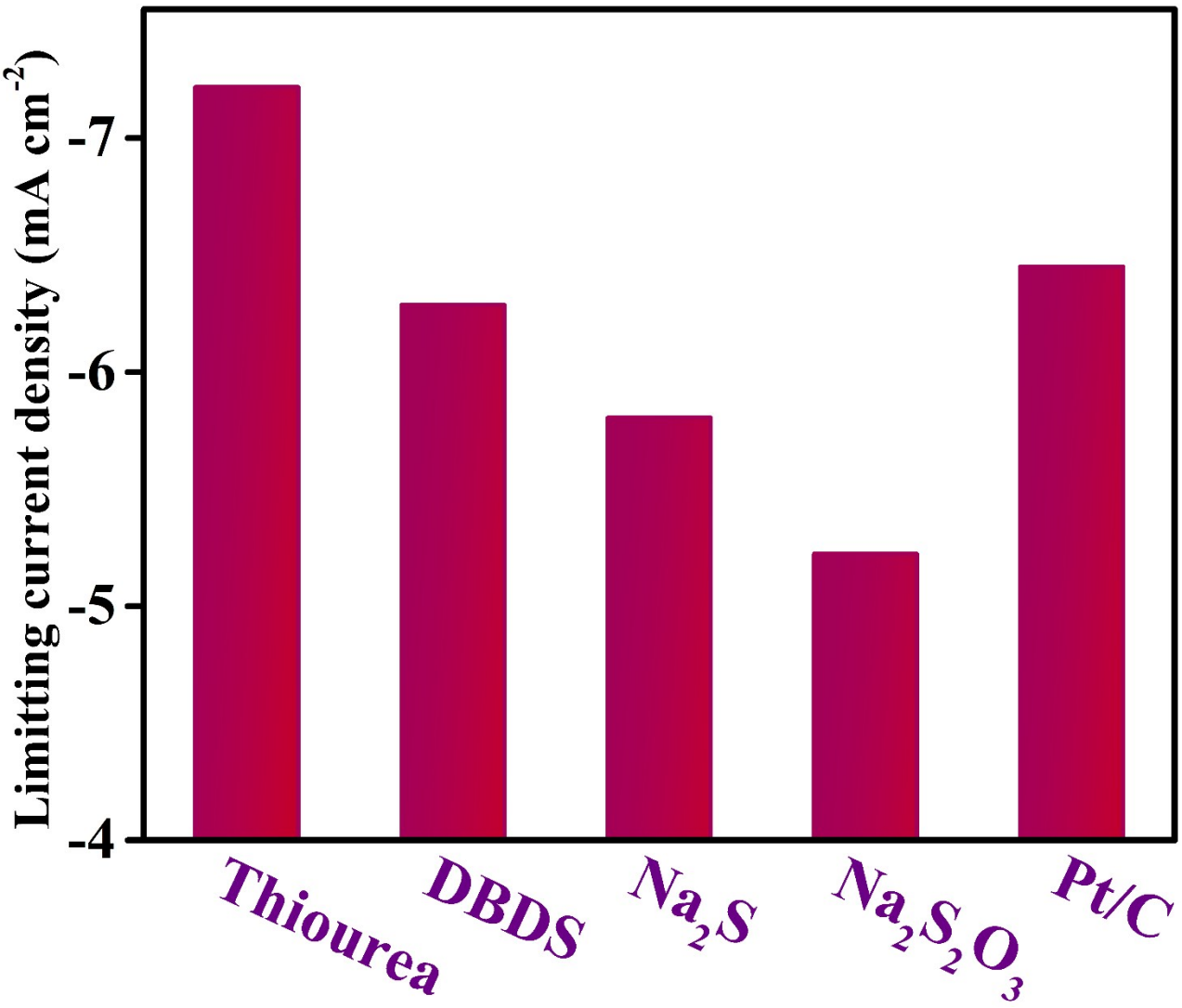

Fig. S20 Comparison of the limiting current densities of Fe–N–C/Fe_3C/C–S–C electrocatalysts prepared from different S precursors.

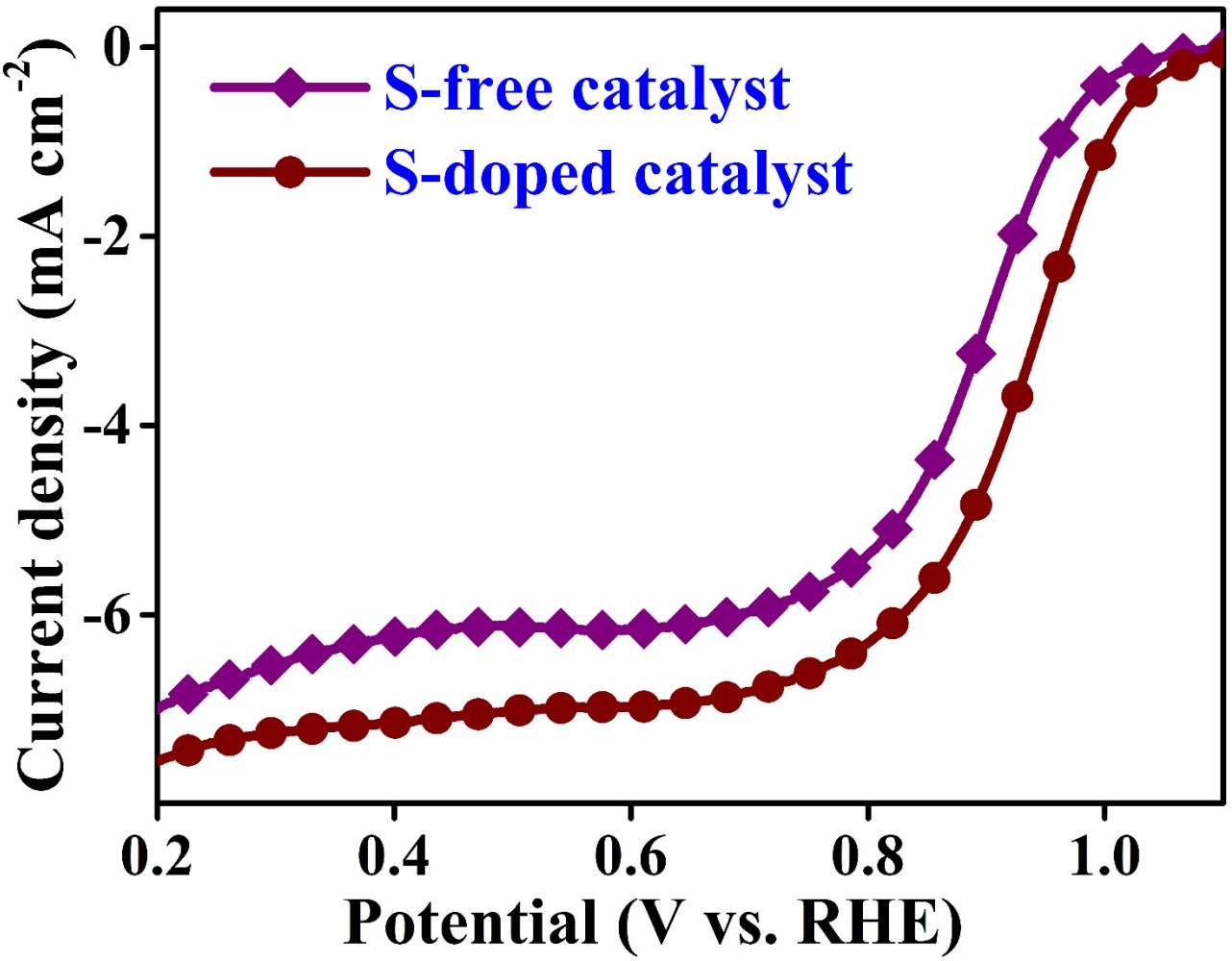

Fig. S21 LSV plots of the S-free and optimized S-doped electrocatalysts, in O_2–saturated 0.10 M KOH electrolyte at scan rate of 5 mV s^{-1} and electrode rotation speed of 1600 rpm.

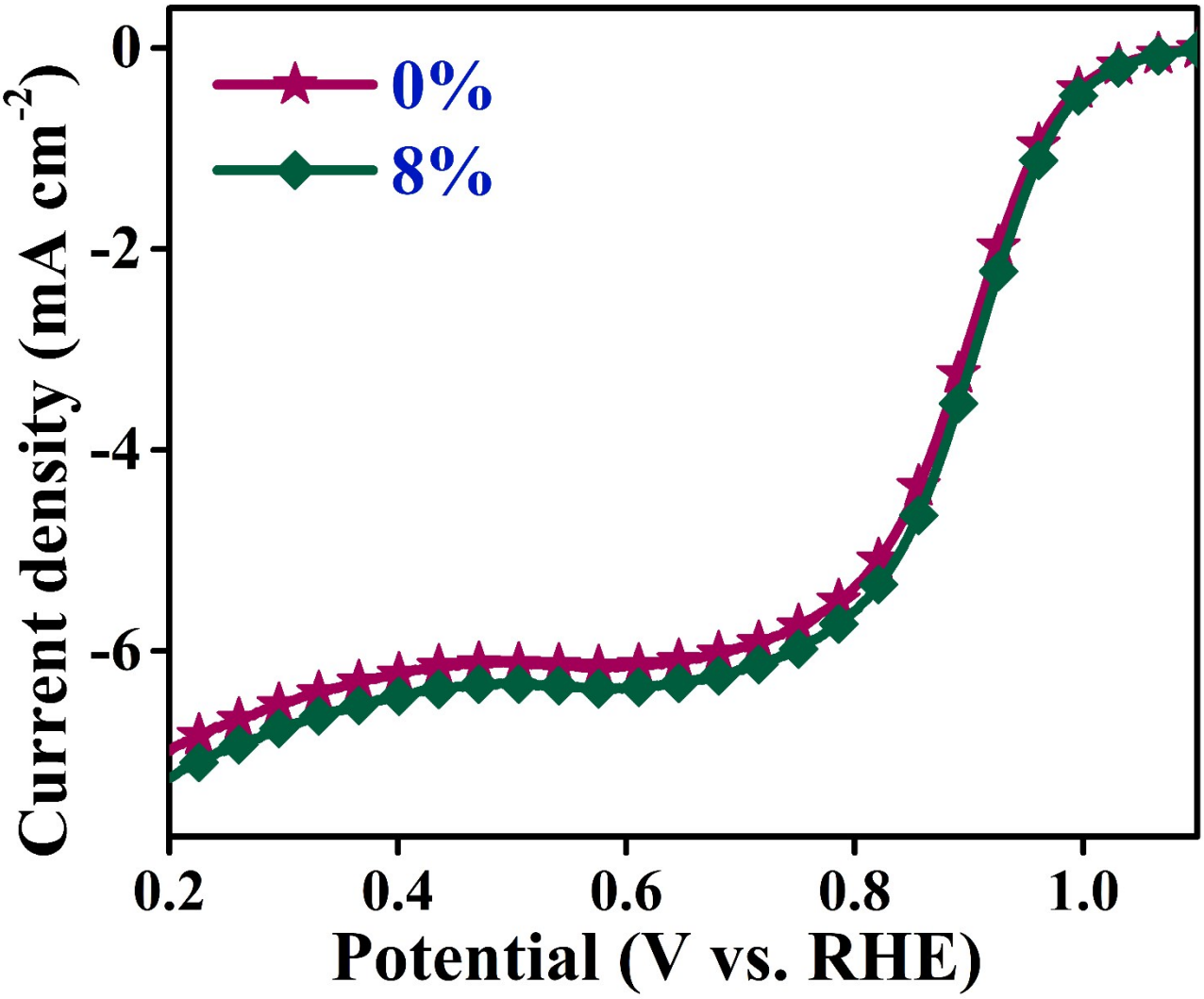

Fig. S22 LSV plots of the electrocatalysts prepared without S-doping and in the presence of 8 wt% of thiourea, in O_2–saturated 0.10 M KOH electrolyte at scan rate of 5 mV s^{-1} and electrode rotation speed of 1600 rpm.

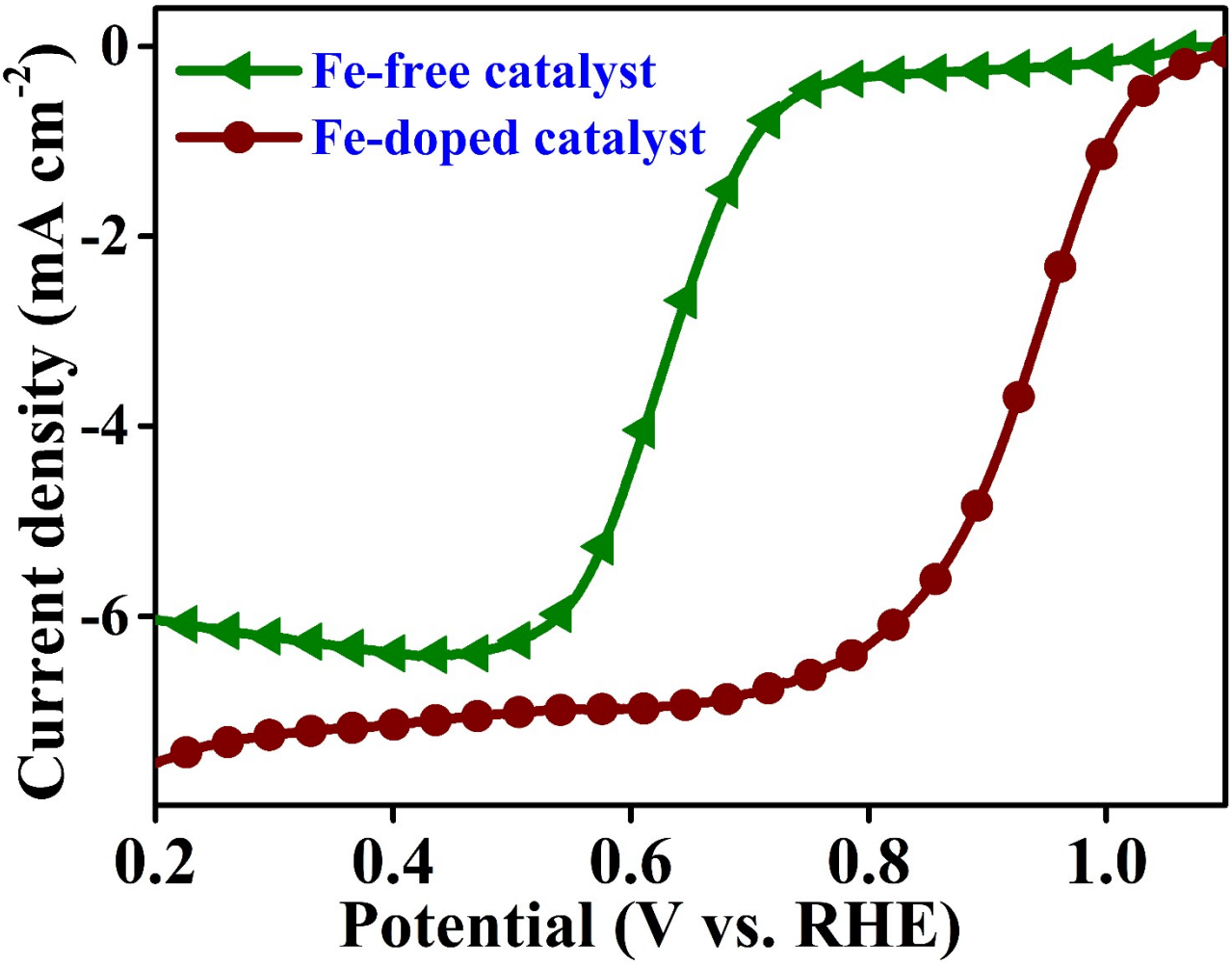

Fig. S23 LSV plots of the Fe-free and Fe-doped electrocatalysts, in O_2–saturated 0.10 M KOH electrolyte at scan rate of 5 mV s^{-1} and electrode rotation speed of 1600 rpm.

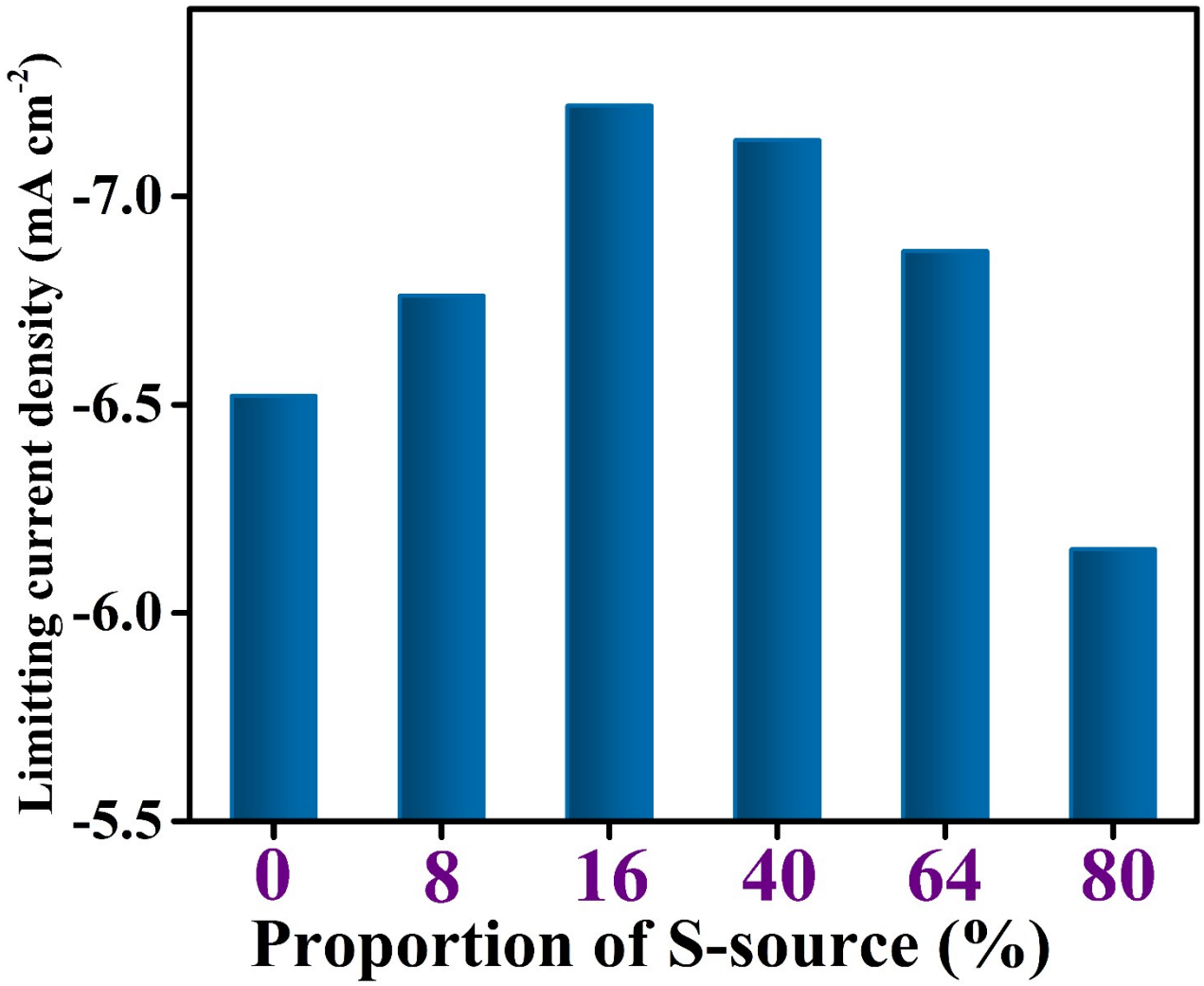

Fig. S24 Comparison of the limiting current densities of Fe–N–C/Fe_3C/C–S–C nanohybrids synthesized in the existence of different weight ratios of thiourea.

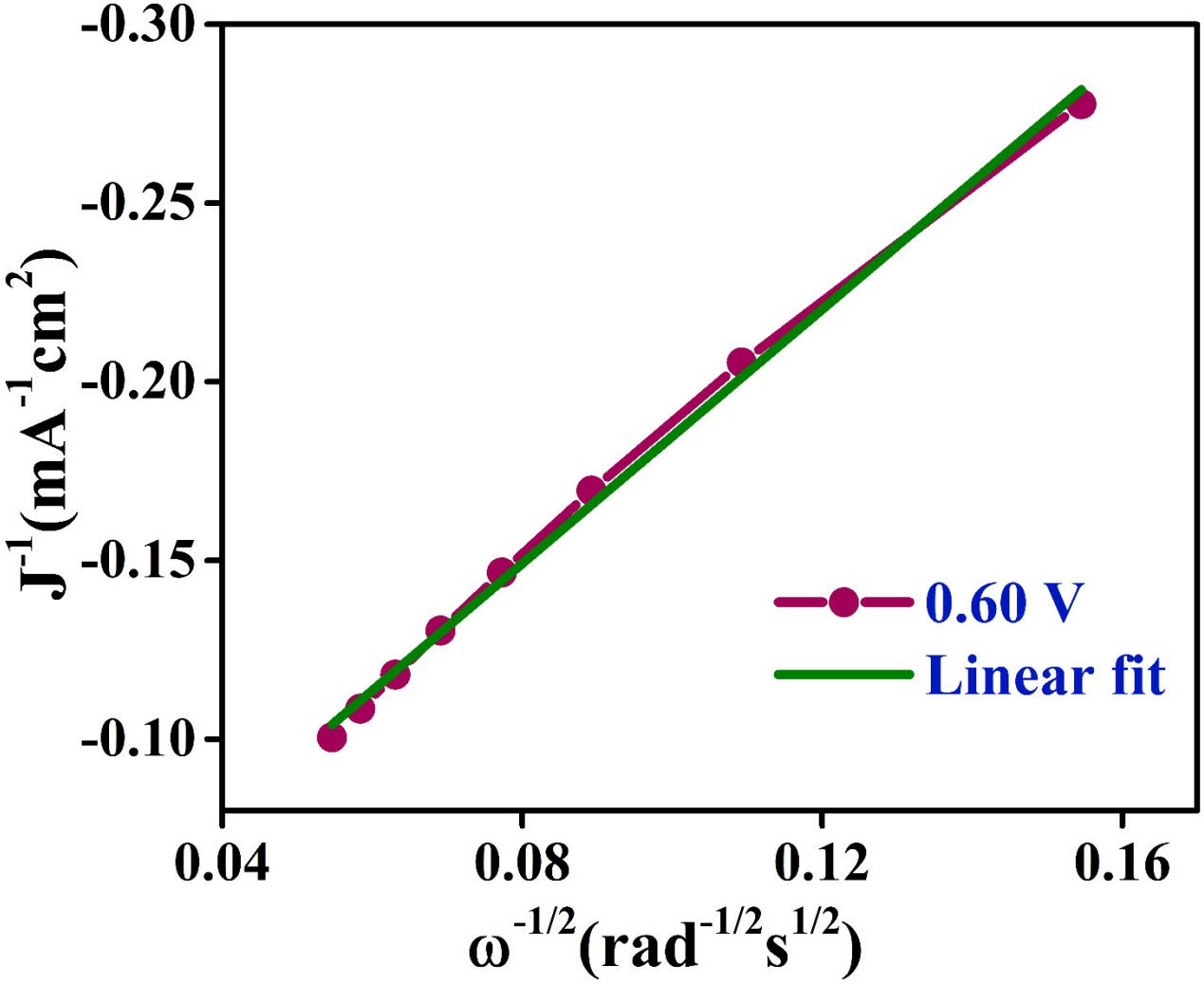

Fig. S25 Linear fit of the K–L plot attained at the potential of 0.60 V for Fe–N–C/Fe_3C/C–S–C nanohybrid, in the basic medium.

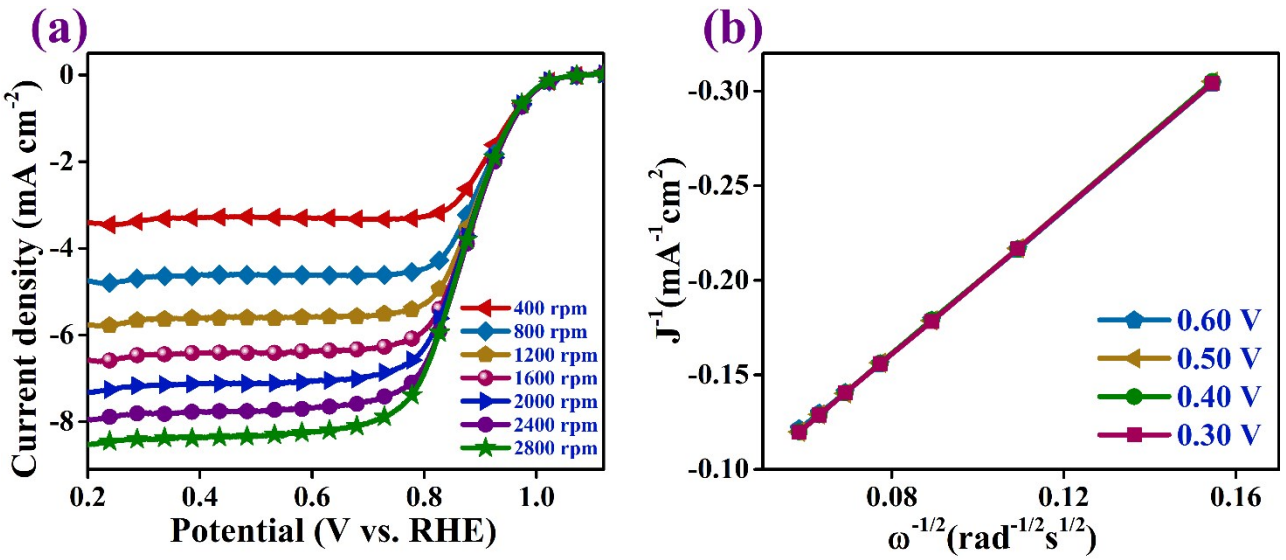

Fig. S26 (a) LSV plots of the benchmark Pt/C (20 wt%) at various electrode rotation rates in O_2–saturated 0.10 M KOH electrolyte at scan rate of 5 mV s^{-1}. (b) Corresponding K–L plots at various potentials.

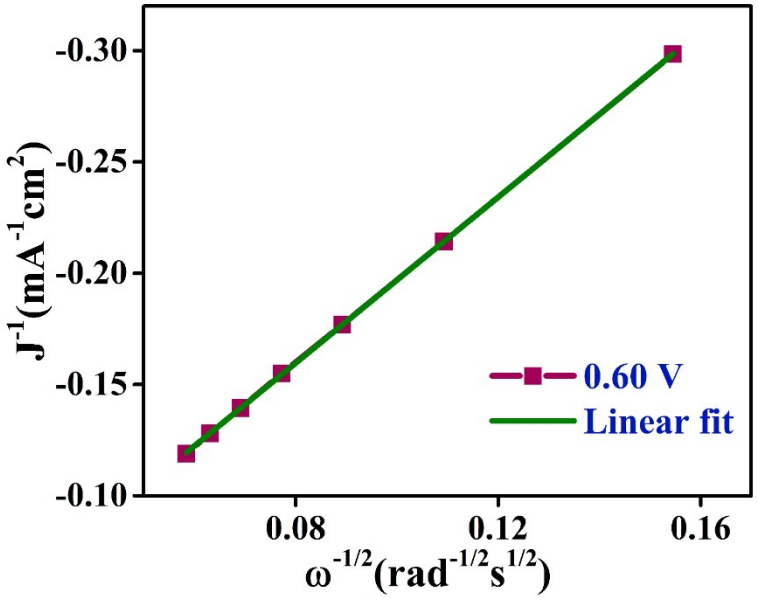

Fig. S27 Linear fit of the K–L plot obtained at the potential of 0.60 V for the commercial Pt/C (20 wt%), in the basic medium.

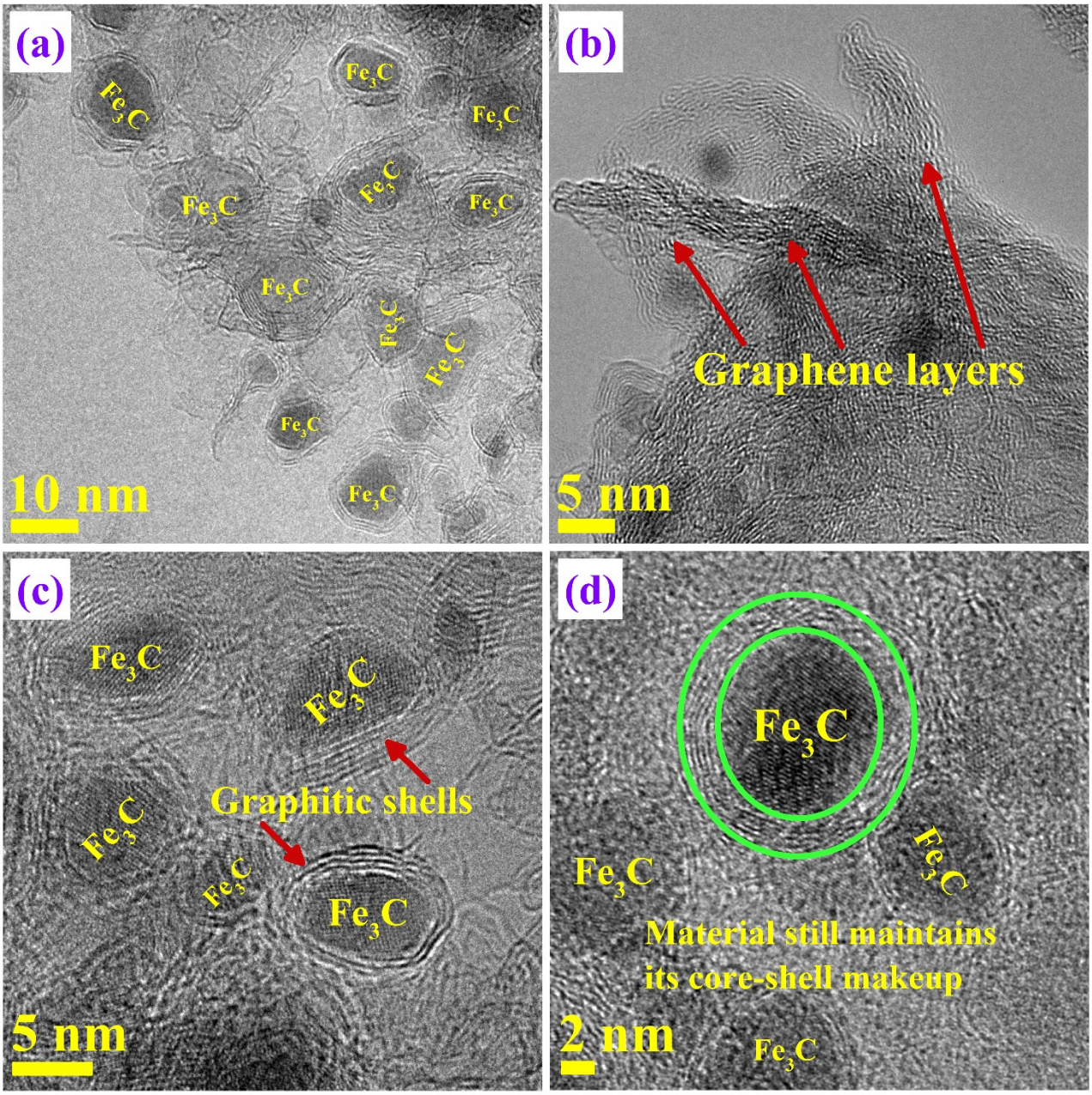

Fig. S28 (a) TEM image, and (b–d) HRTEM images of Fe–N–C/Fe_3C/C–S–C nanohybrid recorded after 15,000 potential cycles in O_2–saturated 0.10 M KOH electrolyte. It is clear that the electrocatalyst still preserves its core-shell nanostructure and the graphitic domains are still obvious even after 15,000 potential cycles, indicating the excellent durability and remarkable resistance to corrosion.

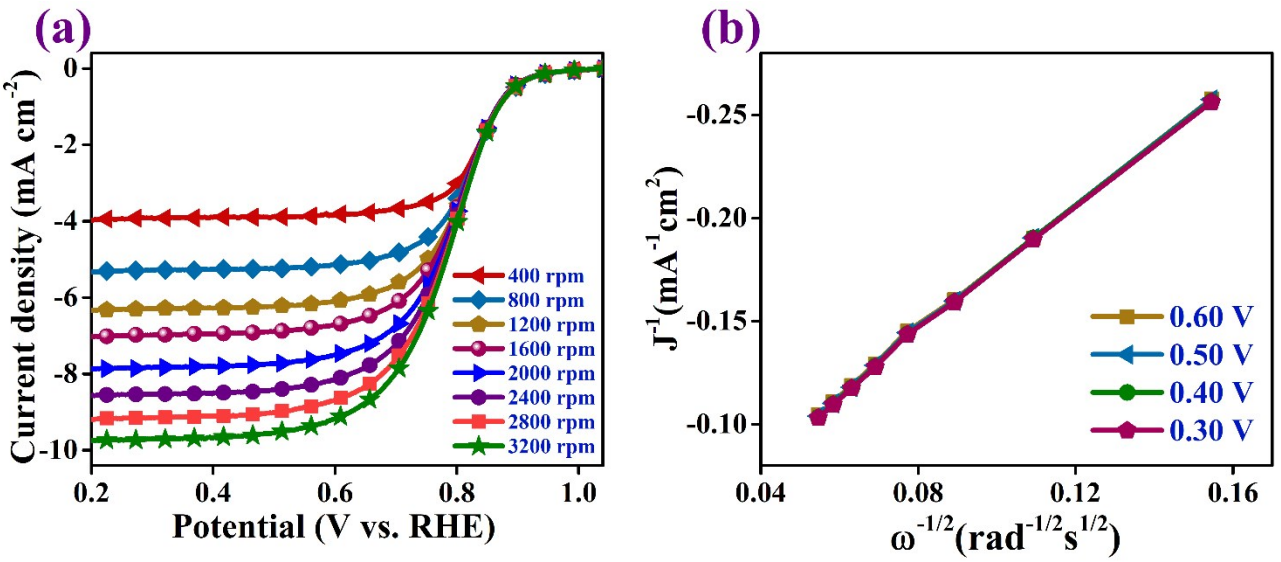

Fig. S29 (a) LSV plots of Fe–N–C/Fe_3C/C–S–C nanohybrid at various electrode rotation velocities, in O_2–saturated 0.10 M $HClO_4$ electrolyte at scan rate of 5 mV s^{-1}. (b) Corresponding K–L plots at various potentials.

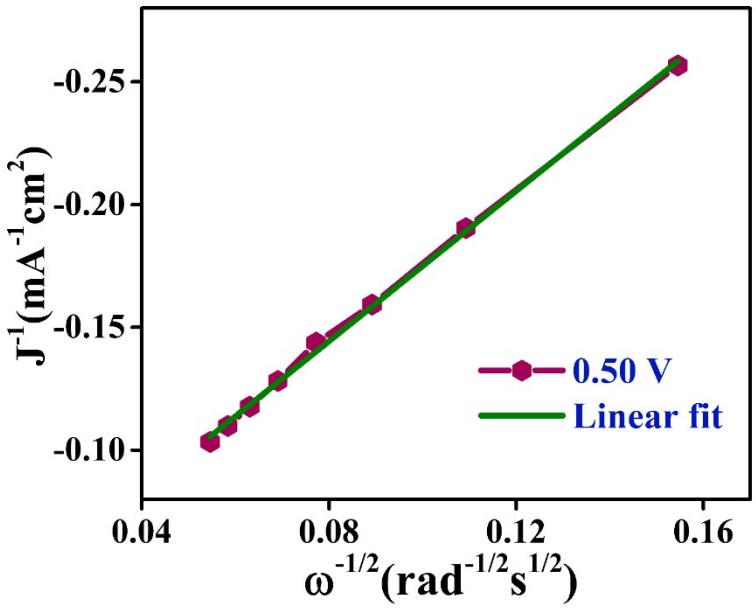

Fig. S30 Linear fit of the K–L plot obtained at the potential of 0.50 V for Fe–N–C/Fe_3C/C–S–C nanohybrid, in the acidic medium.

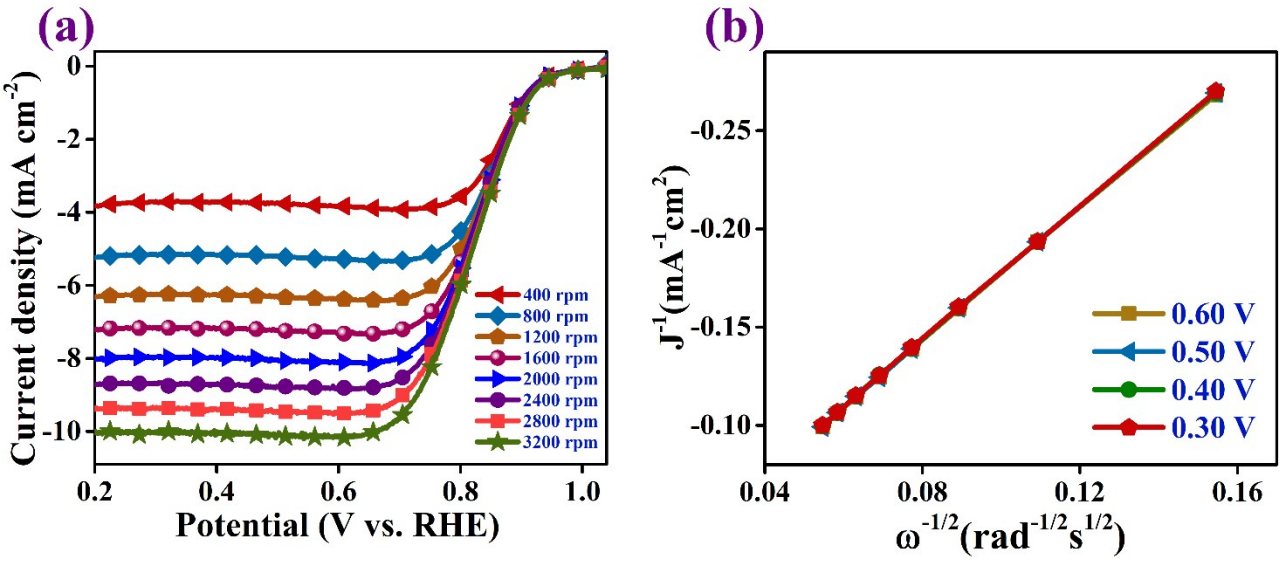

Fig. S31 (a) LSV plots of the state-of-the-art Pt/C (20 wt%) at various electrode rotation speeds, in O_2–saturated 0.10 M $HClO_4$ electrolyte at scan rate of 5 mV s^{-1}. (b) Corresponding K–L plots at various potentials.

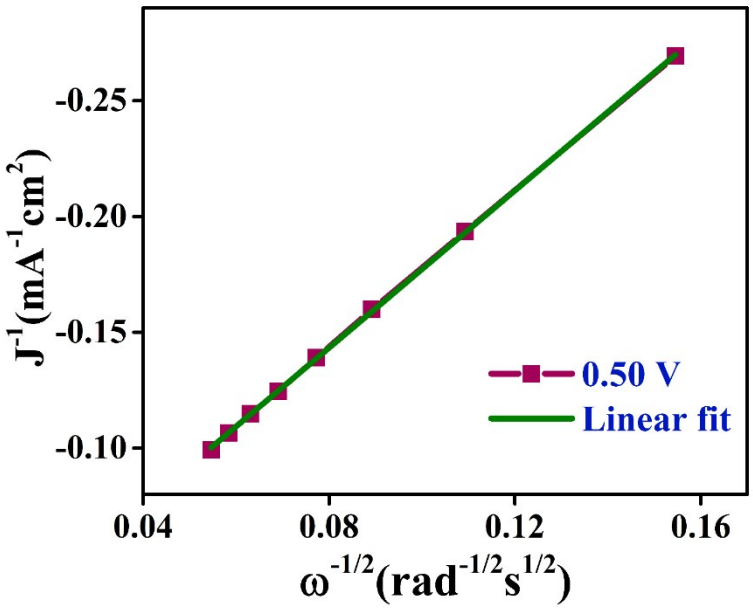

Fig. S32 Linear fit of the K–L plot attained at the potential of 0.50 V for of the state-of-the-art Pt/C (20 wt%), in the acidic medium.

Table S1. Experimental weight percentages of thiourea, 2-cyanoguanidine, sucrose, and ammonium ferric oxalate trihydrate used in fabricating the electrocatalysts.

Thiourea, wt%	2-Cyanoguanidine, wt%	Sucrose, wt%	Fe-source, wt%
0	80	15	5
8	72	15	5
16	64	15	5
40	40	15	5
64	16	15	5
80	0	15	5

Table S2. Micropore surface area (S_{micro}), BET specific surface area (S_{BET}), micropore volume (V_{micro}), total pore volume (V_{tot}), and average pore size (d) of the studied electrocatalysts.

Catalyst[a]	S_{micro} (m^2 g^{-1})	S_{BET} (m^2 g^{-1})	V_{micro} (cm^3 g^{-1})	V_{tot} (cm^3 g^{-1})	d (nm)
1	35	436	0.023	0.452	3.90
2	37	348	0.024	0.299	3.65, 3.85
3	2	51	0.0008	0.112	4.00
4	3	56	0.0009	0.116	3.85
5	31	318	0.018	0.387	3.85
6	29	260	0.015	0.226	3.90
7	2	37	0.0007	0.054	3.90

[a]**1**, **2**, **3**, and **4** are Fe–N–C/Fe_3C/C–S–C electrocatalysts synthesized in the presence of thiourea, DBDS, Na_2S, and $Na_2S_2O_3$, respectively. **5** is the electrocatalyst prepared without S-doping. **6** and **7** are the Fe–N–C/Fe_3C/C–S–C electrocatalysts fabricated using 40 and 80 wt% of thiourea. Note that **1** is also the Fe–N–C/Fe_3C/C–S–C electrocatalyst prepared using 16 wt% of thiourea.

Table S3. Atomic percentages of carbon, nitrogen, sulfur, oxygen, and iron based on the XPS analysis in some of the electrocatalysts synthesized with different sulfur precursors and various proportions of thiourea.

Sample[a]	C (at%)	N (at%)	S (at%)	O (at%)	Fe (at%)
1	85.19	6.47	0.97	6.21	1.16
2	82.72	4.95	1.36	9.64	1.33
3	84.65	2.31	2.18	10.64	0.22
4	85.10	4.17	1.90	7.11	1.72

[a]**1**, **2** and **3** are the Fe–N–C/Fe_3C/C–S–C electrocatalysts synthesized in the presence of thiourea, DBDS, and $Na_2S_2O_3$ precursors, respectively. **4** is the Fe–N–C/Fe_3C/C–S–C electrocatalyst fabricated using 40 wt% of thiourea. Note that **1** is also the Fe–N–C/Fe_3C/C–S–C electrocatalyst prepared using 16 wt% of thiourea.

Table S4. Contents of the various nitrogen bonding configurations in the samples synthesized using different sulfur precursors and various proportions of thiourea. The percentage values have been estimated by calculating the area of each individual peak in the deconvoluted N 1s spectra and comparing it with the overall area of all peaks, then multiplying the obtained number by the total N content for each catalyst.

Sample[a]	Pyridinic-N (at%)	N-Fe (at%)	Pyrrolic-N (at%)	Graphitic-N (at%)	Oxidized-N (at%)
1	1.85	1.49	1.33	1.07	0.73
2	1.14	0.99	1.18	0.91	0.73
3	1.02	0.71	0.58	-	-
4	0.90	0.91	1.02	0.80	0.54

[a]**1**, **2** and **3** are the Fe–N–C/Fe_3C/C–S–C nanohybrids synthesized in the presence of thiourea, DBDS, and $Na_2S_2O_3$ precursors, respectively. **4** is the Fe–N–C/Fe_3C/C–S–C nanohybride fabricated using 40 wt% of thiourea. Note that **1** is also the Fe–N–C/Fe_3C/C–S–C nanohybride prepared using 16 wt% of thiourea.

Table S5. Contents of the various sulfur bonding configurations in the samples synthesized using different sulfur precursors and various proportions of thiourea. The percentage values have been estimated by calculating the area of each individual peak in the deconvoluted S 2p spectra and comparing it with the overall area of all peaks, then multiplying the obtained number by the total S content for each catalyst.

Sample[a]	Fe-S (at%)	S ($2p_{3/2}$) (at%)	S ($2p_{1/2}$) (at%)	Oxidized-S (at%)
1	0.27	0.24	0.18	0.28
2	0.39	0.34	0.25	0.38
3	-	0.55	0.42	1.21
4	0.57	0.46	0.32	0.55

[a]**1**, **2** and **3** are the Fe–N–C/Fe_3C/C–S–C electrocatalysts synthesized in the presence of thiourea, DBDS, and $Na_2S_2O_3$ precursors, respectively. **4** is the Fe–N–C/Fe_3C/C–S–C electrocatalyst fabricated using 40 wt% of thiourea. Note that **1** is also the Fe–N–C/Fe_3C/C–S–C electrocatalyst prepared using 16 wt% of thiourea.

Table S6. Contents of the various iron bonding configurations in the samples synthesized using different sulfur precursors and various proportions of thiourea. The percentage values have been estimated by calculating the area of each individual peak in the deconvoluted Fe 2p spectra and comparing it with the overall area of all peaks, then multiplying the obtained number by the total Fe content for each catalyst.

Sample[a]	Fe^0 (at%)	Fe^{2+} ($2p_{3/2}$) (at%)	Fe–N (at%)	Fe^{3+} ($2p_{3/2}$) (at%)	Fe^{2+} ($2p_{1/2}$) (at%)	Fe^{3+} ($2p_{1/2}$) (at%)
1	0.24	0.24	0.18	0.13	0.13	0.24
2	0.37	0.26	0.22	0.14	0.16	0.18
3	-	0.05	0.03	0.04	0.09	0.01
4	0.62	0.29	0.24	0.14	0.25	0.18

[a]**1**, **2** and **3** are the Fe–N–C/Fe_3C/C–S–C electrocatalysts synthesized in the presence of thiourea, DBDS, and $Na_2S_2O_3$ precursors, respectively. **4** is the Fe–N–C/Fe_3C/C–S–C electrocatalyst fabricated using 40 wt% of thiourea. Note that **1** is also the Fe–N–C/Fe_3C/C–S–C electrocatalyst prepared using 16 wt% of thiourea.

Table S7. Comparison of the ORR performance of Fe–N–C/Fe_3C/C–S–C nanohybrid with recently reported high-performance nonprecious electrocatalysts in alkaline medium.

Electrocatalyst	Onset potential (V)	Half-wave potential (V)	Electron transfer Number	Reference
Fe–N–C/Fe_3C/C–S–C	**1.078**	**0.929**	**4.03**	**This work**
Pt/C (20 wt%)	**1.034**	**0.889**	**3.98**	**This work**
Fe_2N/NC	1.10	0.91	-	*ACS Catal.* **2020**, 10, 2443−2451
FeCo–C/N	-	0.864	3.88	*J. Mater. Chem. A*, **2020**, 8, 9536–9544
Fe–N–C	1.01	0.930	3.98	*Adv. Mater.* **2020**, 32, 1907399
Fe/OES	1.0	0.85	4	*Angew. Chem. Int. Ed.* **2020**, 59, 7384–7389
Fe–N/P–C–700	0.941	0.867	3.94	*J. Am. Chem. Soc.* **2020**, 142, 2404−2412
Fe–N–C	-	0.915	4	*ACS Catal.* **2020**, 10, 2452−2458
Fe–N/GNs	-	0.903	4.05	*Small Methods* **2020**, 1900827
Co−N_3C_1@GC	0.904	0.824	4	*ACS Catal.* **2020**, 10, 5862−5870
Fe_x−N−C	-	0.920	4	*J. Am. Chem. Soc.* **2019**, 141, 2035−2045
Zn/CoN–C	1.004	0.861	3.88	*Angew. Chem.* **2019**, 131, 2648–2652
mC–TpBpy–Fe	0.92	0.845	4	*Chem. Mater.* **2019**, 31, 3274−3280
Fe,N–HPCC	0.972	0.898	4	*Nano Energy* **2019**, 57, 108–117
Fe@FeNC	0.946	0.852	3.78	*Appl. Catal. B Environ.* **2019**, 251, 240–246
h–FeNC	0.996	0.883	3.88	*J. Mater. Chem. A*,

				2019, 7, 12518–12525
Fe−NCNWs	-	0.91	3.98	*ACS Catal.* **2019**, 9, 5929−5934
BMOF−CoFe	-	0.89	3.9	J. *Am. Chem. Soc.* **2019**, 141, 10744–10750
Fe_{AC}@Fe_{SA}−N−C	-	0.912	4	*ACS Nano* **2019**, 13, 11853−11862
$Mn_{0.8}(CoFe_2)_{0.73}O_4$	-	0.89	-	*J. Am. Chem. Soc.* **2019**, 141, 4412−4421
$NiCo_2S_4$@g–C_3N_4–CNT	0.87	0.76	4	*Adv. Mater.* **2019**, 31, 1808281
Co–N–C/CoO_x	0.89	0.82	3.9	*Small* **2019**, 15, 1804855
Fe SAs/N–C	-	0.91	4	*ACS Catal.* **2019**, 9, 2158−2163
Fe/Fe_3C@C_4N	-	0.884	3.92	*Nano Energy* **2019**, 56, 581–587
Fe–N–C	1.0	0.90		*Nano Energy* **2019**, 61, 60–68
Fe–N/CNT	-	0.922	3.98	*Adv. Funct. Mater.* **2019**, 1906174
Co–Fe/NC	-	0.854	3.81	*Small* **2019**, 1805324
Fe/Fe_5C_2@N–C	-	0.85	3.84	*Appl. Catal. B Environ.* **2019**, 244, 197–205
Fe/N/S–PCNT	0.96	0.84	3.94	*J. Mater. Chem. A* **2019**, 7, 1607–1615
Mn–Fe–N/S@mC	-	0.896	3.9	*Nano Energy* **2019**, 63, 103851
FeNGC–T	1.03	0.88	3.98	*J. Mater. Chem. A* **2019**, 7, 20132–20138
Cu–Fe–N–C	0.967	0.864	4	*Appl. Catal. B Environ.* **2019**, 242, 209–217
FeZ–CNS	0.963	0.881	3.95	*J. Mater. Chem. A* **2019**, 7, 11223–11233

Co–Fe/NC	-	0.854	3.81	*Small* **2019**, 1805324
Fe–N–S CNN	-	0.91	4	*Appl. Catal. B Environ.* **2019**, 250, 143–149
Fe–N/C	-	0.85	4	*J. Mater. Chem. A* **2019**, 7, 16508–16515
PcCu–O_8–Co	-	0.83	3.93	*Angew. Chem. Int. Ed.* **2019**, 58, 10677–10682
FeNCNs	0.985	0.890	3.9	*J. Mater. Chem. A* **2019**, 7, 11792–11801

Table S8. Comparison of the ORR performance of Fe–N–C/Fe_3C/C–S–C nanohybrid with recently reported high-performance nonprecious electrocatalysts in acidic medium.

Electrocatalyst	Onset potential (V)	Half-wave potential (V)	Electron transfer number	Reference
Fe–N–C/Fe_3C/C–S–C	**0.956**	**0.812**	**3.95**	**This work**
Pt/C (20 wt%)	**0.961**	**0.836**	**3.97**	**This work**
Fe_3O_4@NC/NHPC	0.898	0.803	3.91	*Adv. Sci.* **2020**, 2000407
Fe–N_4	-	0.80	4	*Adv. Mater.* **2020**, 32, 2000966
Fe–N/GNs	-	0.837	3.91	*Small Methods* **2020**, 1900827
Fe–N–C_{950}	-	0.80	4	*J. Am. Chem. Soc.* **2020**, 142, 5477−5481
Fe–N/P–C–700	0.89	0.72	3.93	*J. Am. Chem. Soc.* **2020**, 142, 2404−2412
Fe–N–C	-	0.76	-	*Adv. Mater.* **2020**, 32, 1907399
Fe/N/S–PCNT	0.80	0.62	3.84	*J. Mater. Chem. A* **2019**, 7, 1607–1615
H−FeCo−N_x−C	0.943	0.75	3.7	*ACS Nano* **2019**, 13, 8087−8098
Co@SNHC	0.852	0.682	3.90	*J. Mater. Chem. A* **2019**, 7, 14291–14301
Fe,N–HPCC	-	0.76	3.99	*Nano Energy* **2019**, 57, 108–117
FeN_x/GM	-	0.80	-	*Adv. Energy Mater.* **2019**, 1803737
Fe–N/CNT	-	0.753	-	*Adv. Funct. Mater.* **2019**, 1906174
Fe–N–C	-	0.78	4	*Appl. Catal. B Environ.* **2019**, 259, 118042–118049

Fe–N–C	0.95	0.81	4	*Nano Energy* **2019**, 61, 60–68
FeNGC–T	0.90		3.90	*J. Mater. Chem. A* **2019**, 7, 20132–20138
Fe SAs/N–C	-	0.798	3.97	*ACS Catal.* **2019**, 9, 2158−2163
Fe/Fe_5C_2@N–C	-	0.66	-	*Appl. Catal. B Environ.* **2019**, 244, 197–205
FeZ–CNS	0.820	0.720	3.8	*J. Mater. Chem. A* **2019**, 7, 11223–11233
Zn/CoN–C	0.97	0.796	-	*Angew. Chem.* **2019**, 131, 2648 –2652
Fe−NCNWs	-	0.82	3.98	*ACS Catal.* **2019**, 9, 5929−5934
Fe–N–S CNN	-	0.78	4	*Appl. Catal. B Environ.* **2019**, 250, 143–149
CNT–Fe/NHCNS	-	0.84	3.93	*J. Mater. Chem. A* **2019**, 7, 14478–14482